

Modeling Nonstationary Extremal Dependence via Deep Spatial Deformations

Xuanjie Shao¹, Jordan Richards², and Raphaël Huser¹

¹Statistics Program, Computer, Electrical and Mathematical Sciences and Engineering (CEMSE) Division, King Abdullah University of Science and Technology (KAUST), Thuwal 23955-6900, Saudi Arabia

²School of Mathematics and Maxwell Institute for Mathematical Sciences, University of Edinburgh, Edinburgh, EH9 3FD, UK

Abstract

Modeling nonstationarity that often prevails in extremal dependence of spatial data can be challenging, and typically requires bespoke or complex spatial models that are difficult to estimate. Inference for stationary and isotropic models is considerably easier, but the assumptions that underpin these models are rarely met by data observed over large or topographically complex domains. A possible approach for accommodating nonstationarity in a spatial model is to warp the spatial domain to a latent space where stationarity and isotropy can be reasonably assumed. Although this approach is very flexible, estimating the warping function can be computationally expensive, and the transformation is not always guaranteed to be bijective, which may lead to physically unrealistic transformations when the domain folds onto itself. We overcome these challenges by developing deep compositional spatial models to capture nonstationarity in extremal dependence. Specifically, we focus on modeling high threshold exceedances of process functionals by leveraging efficient inference methods for limiting r -Pareto processes. A detailed high-dimensional simulation study demonstrates the superior performance of our model in estimating the warped space. We illustrate our method by modeling UK precipitation extremes and show that we can efficiently estimate the extremal dependence structure of data observed at thousands of locations.

Keywords: Deep Learning, Nonstationarity, r -Pareto Process, Spatial Extremes

1 Introduction

The most impactful extreme events, such as Storm Dennis, which brought record-breaking rainfall leading to severe flooding across the UK (Sefton et al., 2021), are often spatial in

nature; therefore, there is a critical need to account for spatial extremal dependence when assessing the risk of unprecedented environmental extremes. Natural processes observed over large geographical domains are often inhomogeneous due to orography or proximity to the coast, among other factors, and capturing such (potentially complex) nonstationary behavior prevailing in both margins and dependence can be challenging. Failing to adequately model this nonstationarity can lead to poor risk assessment and suboptimal mitigation strategies. Herein, we focus on modeling nonstationarity in spatial dependence. Various modeling approaches have been proposed to account for nonstationarity in the extremal dependence structure of spatial processes; they can be generally categorized into two major classes: i) those that directly impose nonstationarity in the extremal dependence structure itself (Huser and Genton, 2016; Saunders et al., 2021; Forster and Oesting, 2025; Shao et al., 2025), and ii) those that rely on a deformation of the spatial domain to capture nonstationarity (Youngman, 2020; Chevalier et al., 2021; Richards and Wadsworth, 2021).

For the first class of models, nonstationarity is often incorporated into the covariance function (or variogram) of an underlying Gaussian process used in the model construction, which induces nonstationarity in the resulting model’s extremal dependence structure. An important consideration, therefore, is to create flexible nonstationary covariance functions that retain positive definiteness. One possible approach is to exploit the Paciorek and Schervish (2006) covariance model, which defines a globally nonstationary model through simpler local (spatially-varying) covariance kernels. Covariates can then easily be incorporated into local range and anisotropy parameters (Huser and Genton, 2016). However, a covariate-based approach often lacks the flexibility to capture complex nonstationary behaviors. Balancing model flexibility and parsimony is indeed pivotal, and various approaches have been proposed to deal with this trade-off. A popular approach involves regionalization of the study domain into multiple homogeneous subregions, with some subregions enforced to share similar extremal dependence behavior, through equal dependence parameters. Buhl and Klüppelberg (2016) and Saunders et al. (2021) proposed to identify the subregions by clustering sites using information about their extremal dependence structure. Shao et al. (2025) instead advocated a spatially-motivated penalized estimation

procedure to identify homogeneous subregions; similar methods have also been proposed in classical geostatistics (see, e.g., [Parker et al., 2016](#)). For modeling stationary but anisotropic dependence, a common choice is to use a parametric anisotropic covariance function or variogram, where the notion of distance considers the relative orientation of stations (see, e.g., [Huser and Genton, 2016](#); [de Fondeville and Davison, 2018](#)).

Instead of directly modeling nonstationary dependence via complex parametrizations of covariance/variogram functions, the spatial deformation approach, proposed by [Sampson and Guttorp \(1992\)](#), warps the original spatial domain into a latent space where stationarity and isotropy of data can be reasonably assumed. Estimation of the warping function is challenging: this task may be computationally expensive; the chosen class of warping functions may lack flexibility (especially in cases when there is strong nonstationarity); or, conversely, the model may be too flexible and overfit the data. The estimated warping may also display the notorious problem of “space-folding” if not appropriately constrained, which is undesirable and implausible for environmental data ([Schmidt and O’Hagan, 2003](#)). To estimate the warping function $\mathbf{f} : \mathcal{S} \rightarrow \mathcal{W}$ from the original spatial domain $\mathcal{S} \subseteq \mathbb{R}^K$ to the latent space $\mathcal{W} \subseteq \mathbb{R}^K$ (typically with $K = 2$ or $K = 3$), [Sampson and Guttorp \(1992\)](#) exploited multidimensional scaling; this approach was extended by [Chevalier et al. \(2021\)](#) for the modeling of nonstationary extremal dependence. [Smith \(1996\)](#) instead adopted a spline-based approach for modeling the warping function in the Gaussian setting, followed by [Youngman \(2020\)](#) and [Richards and Wadsworth \(2021\)](#) in the extremal setting, with practical techniques advocated to reduce the chance of estimating non-bijective warpings (i.e., “space-folding”). Bayesian hierarchical models were also considered by [Schmidt and O’Hagan \(2003\)](#), where the warping function $\mathbf{f}(\cdot)$ was modeled as a bivariate Gaussian process, thus precluding non-bijective warpings via specification of suitable priors.

To fully preclude space-folding, [Perrin and Monestiez \(1999\)](#) and [Iovleff and Perrin \(2004\)](#) used a composition of bijective radial basis functions to model $\mathbf{f}(\cdot)$; [Zammit-Mangion et al. \(2022\)](#) further developed the deep compositional spatial model (DCSM), a bijective warping model constructed from a composition of simple bijective warping units. Specifically, suppose $X(\cdot)$ is a spatial process on some spatial domain $\mathcal{S} \subseteq \mathbb{R}^K$. The spatial

deformation approach assumes that on the latent warped space $\mathcal{W} \subseteq \mathbb{R}^K$, the dependence structure solely depends on the Euclidean distance, i.e., $\|\mathbf{f}(\mathbf{s}_1) - \mathbf{f}(\mathbf{s}_2)\|$, but not on the individual sites $\mathbf{s}_1, \mathbf{s}_2 \in \mathcal{S}$. Deep compositional spatial models further construct the warping function $\mathbf{f}(\cdot)$ using a composition $\mathbf{f}(\cdot) = \mathbf{f}_n \circ \mathbf{f}_{n-1} \circ \cdots \circ \mathbf{f}_1(\cdot)$ of simple bijective warping functions $\mathbf{f}_i : \mathcal{W}_{i-1} \rightarrow \mathcal{W}_i$, where $\mathcal{W}_{i-1} \subseteq \mathbb{R}^K$ is the domain of $\mathbf{f}_i(\cdot)$ and $\mathcal{W}_i \subseteq \mathbb{R}^K$ is its image; here, $\mathcal{W}_0 := \mathcal{S}$ is the original space, $\{\mathcal{W}_i, i = 1, \dots, n-1\}$ are intermediate warped spaces, and $\mathcal{W}_n := \mathcal{W}$ is the final warped space. The simple functions $\mathbf{f}_i(\cdot)$ may be specified, for example, as axial warping units, radial basis functions, or based on the Möbius transform (see Section 2.2 for details), and they may differ across $i = 1, \dots, n$. By using efficient inferential techniques designed for deep learning, the DCSM can efficiently handle high dimensional data, i.e., observations over a large number D of locations, and estimate a highly flexible warping with the theoretical guarantee of bijectivity. With efficient optimization software, the modeling capability of the DCSM has been extended to much higher-dimensional settings than was previously possible using alternative approaches. While [Zammit-Mangion et al. \(2022\)](#) originally developed the DCSM for univariate spatial Gaussian processes, [Vu et al. \(2022, 2023\)](#) further extended this framework to multivariate and space-time Gaussian processes, but they did not consider non-Gaussian settings. The number of parameters describing the warping function in DCSMs is typically quite large; as a result, they can flexibly capture a wide range of nonstationary features. A sufficiently flexible mapping from \mathbb{R}^K to itself makes realistic and comprehensible kriging possible and enhances the interpretability of the estimated space (see [Zammit-Mangion et al., 2022](#) for details), relative to models based on dimensional expansion (see, e.g., [Bornn et al., 2012](#); [Chevalier et al., 2021](#)). To mitigate the risk of overfitting, one can either increase the model’s flexibility progressively by adding warping units step-by-step or use suitable regularization techniques. While [Zammit-Mangion et al. \(2022\)](#) used the former approach, in this work we use the latter.

To model spatial extremal dependence, a popular approach has been to use parametric max-stable processes (see, e.g., [Brown and Resnick, 1977](#); [Smith, 1990](#); [Schlather, 2002](#); [Opitz, 2013](#)), amongst which the Brown–Resnick class is one of the most popular choices.

Although they have proven a useful tool for modeling nonstationary and anisotropic spatial extremal dependence (see, e.g., [Huser and Genton, 2016](#); [Chevalier et al., 2021](#); [Shao et al., 2025](#)), the use of max-stable processes in environmental applications has been criticized, because they are not designed to describe the spatial extreme events that actually occurred but, rather, spatial maxima representing composite spatial extreme events that occurred at different times (see [Huser et al., 2025](#) for an extensive review of their limitations). Peaks-over-threshold models based on Pareto processes offer a more suitable alternative since they allow modeling the original extreme events directly. [Ferreira and de Haan \(2014\)](#) introduced the generalized Pareto process, with spatial exceedances defined using the sup-norm; that is, a process is termed extreme if it is large at at least one site. This class of models was extended by [Dombry and Ribatet \(2015\)](#) to model high threshold exceedances defined in terms of a general nonnegative and homogeneous risk functional (e.g., the spatial average), here denoted by $r(\cdot)$, applied to the spatial process. These so-called r -Pareto processes offer more flexibility in defining spatial extreme events. [de Fondeville and Davison \(2018\)](#), with extension to generalized r -Pareto processes by [de Fondeville and Davison \(2022\)](#), proposed computationally-efficient inference methods for r -Pareto processes constructed from log-Gaussian random functions, which share similar properties with Brown–Resnick max-stable processes. Their approach leverages the gradient scoring rule ([Hyvärinen and Dayan, 2005](#)), which bypasses the computational bottlenecks of likelihood-based inference methods and thus allows r -Pareto models to be fitted to high-dimensional data. Due to their flexibility in defining spatial extremes with various risk functionals and the efficient algorithm available for their inference, we here use r -Pareto processes—combined with the DCSM—to capture nonstationary extremal dependence.

Our contributions can be summarized as follows. We construct deep spatial deformations for peaks-over-threshold events by leveraging, extending, and integrating the DCSM methodology into r -Pareto processes, to flexibly model nonstationary extremal dependence; to this end, we exploit efficient inference methods within a deep learning framework, allowing us to jointly estimate the warping function $\mathbf{f}(\cdot)$ and all other dependence parameters simultaneously in high dimensions. Precisely, inference proceeds either via a least squares

minimization scheme (similar to [Richards and Wadsworth, 2021](#)) or via gradient score matching ([de Fondeville and Davison, 2018](#)). Regularization strategies to preclude overfitting are also explored, and the effect of different risk functionals, $r(\cdot)$, on the estimated extremal dependence pattern is investigated. Our proposed methodology is programmed using a convenient R interface to `Tensorflow` version 2.11.0.

The paper is organized as follows. In [Section 2](#), we develop deep compositional r -Pareto processes to model nonstationary extremal dependence. In [Section 3](#), we detail our joint inference approach for simultaneously estimating the warping function and model parameters. In [Section 4](#), we conduct a detailed simulation study to validate the efficacy of our proposed methodology. In [Section 5](#), we analyze United Kingdom (UK) precipitation extremes and investigate nonstationary extremal dependence patterns of rainfall anomalies around Wales. The proposed modeling approach is found to capture the nonstationarity in the extremal dependence structure well, while facilitating inference with thousands of spatial locations. [Section 6](#) concludes with some discussion.

2 Modeling with deep compositional r -Pareto processes

2.1 r -Pareto process construction

Let $\{Y(\mathbf{s}), \mathbf{s} \in \mathcal{S}\}$ be our process of interest, defined on the compact spatial domain $\mathcal{S} \subseteq \mathbb{R}^K$, and let $F_{\mathbf{s}}(y)$ denote its marginal distribution (assumed continuous) at site $\mathbf{s} \in \mathcal{S}$. Since we focus on modeling the extremal dependence structure of Y , we can consider, without loss of generality, the standardized process $\{X(\mathbf{s}), \mathbf{s} \in \mathcal{S}\}$, obtained as $X(\mathbf{s}) = 1/[1 - F_{\mathbf{s}}\{Y(\mathbf{s})\}]$, which has standard Pareto margins, i.e., $\mathbb{P}(X(\mathbf{s}) > x) = 1/x$, $x \geq 1$, for all $\mathbf{s} \in \mathcal{S}$. There are multiple ways to define spatial extreme events of X . From the peaks-over-threshold perspective, [Ferreira and de Haan \(2014\)](#) defined X to be extreme if $\sup_{\mathbf{s} \in \mathcal{S}}\{X(\mathbf{s})\} \geq u$ for some large threshold $u > 1$. They showed that, under mild assumptions, the only possible limit of the rescaled process X/u given $\sup_{\mathbf{s} \in \mathcal{S}}\{X(\mathbf{s})\} \geq u$, as u tends to infinity, is the so-called simple Pareto process, $\{Z(\mathbf{s}), \mathbf{s} \in \mathcal{S}\}$, which admits

the following construction:

$$Z(\mathbf{s}) = UV(\mathbf{s}), \quad \mathbf{s} \in \mathcal{S}, \quad (1)$$

where U is a standard Pareto random variable and $\{V(\mathbf{s}), \mathbf{s} \in \mathcal{S}\}$ is a nonnegative stochastic process independent of U and satisfying $\sup_{\mathbf{s} \in \mathcal{S}} V(\mathbf{s}) = 1$. This definition of a spatial extreme event using the sup-norm is quite restrictive in practice, as the process Y (or X) is generally not observed throughout the domain \mathcal{S} . To mitigate this issue, [Dombry and Ribatet \(2015\)](#) studied limits of high threshold exceedances defined in terms of a more general nonnegative 1-homogeneous risk functional $r(\cdot)$ (i.e., $r(c \times \cdot) = cr(\cdot)$, for all $c > 0$). A process X is now considered to be extreme if $r(X) \geq u$ for some large threshold $u > 1$, and we say that $X \mid r(X) \geq u$ is an r -exceedance above the threshold u . Under mild assumptions, [Dombry and Ribatet \(2015\)](#) showed that the only possible limit of the rescaled process X/u given that $r(X) \geq u$, as u tends to infinity, is the so-called simple r -Pareto process, i.e.,

$$\mathbb{P}\{u^{-1}X \in \cdot \mid r(X) \geq u\} \rightarrow \mathbb{P}(Z \in \cdot) \text{ as } u \rightarrow \infty, \quad (2)$$

where the limiting process Z has a similar construction as in (1) but with the constraint that $r(V) = 1$ instead. To satisfy the latter condition, one may take $V = Q/r(Q)$ for some nonnegative stochastic process $\{Q(\mathbf{s}), \mathbf{s} \in \mathcal{S}\}$. An essential property of r -Pareto processes is peaks-over-threshold stability (see [Dombry and Ribatet, 2015](#)), also called threshold invariance by [de Fondeville and Davison \(2018\)](#). This means that for any measurable set $\mathcal{A} \subset \{Z : r(Z) \geq 1\}$ and $u > 1$, a simple r -Pareto process satisfies $\mathbb{P}\{u^{-1}Z \in \mathcal{A} \mid r(Z) \geq u\} = \mathbb{P}(Z \in \mathcal{A})$, which can be exploited for joint tail extrapolation.

Risk functionals of practical interest include, among others: i) the max-functional, $r_{\max}(X) := \max_{\mathbf{s} \in \mathcal{D}} X(\mathbf{s})$, which defines extremes such that the process is large at at least one site within a finite subset $\mathcal{D} \subset \mathcal{S}$ —in practice, \mathcal{D} is often chosen as the set of observed sampling locations or a subset thereof; ii) the sum-functional, $r_{\text{sum}}(X) := \sum_{\mathbf{s} \in \mathcal{D}} X(\mathbf{s})$, which defines extremes as events such that the process is large on average over \mathcal{D} ; and iii) the site-functional, $r_{\text{site}}(X) := X(\mathbf{s}_0)$, which is a special case of the max- and sum-functionals

when $\mathcal{D} = \{\mathbf{s}_0\}$ contains a single specific site of interest. For practical applications of the sum-functional, [de Fondeville and Davison \(2018\)](#) argued that a direct summation of the rescaled process X on the standard Pareto scale may not be physically meaningful, and proposed using a modified sum-functional that first transforms the tail of X to match that of the original process Y before computing the sum. Precisely, for some parameter $\beta > 0$, they defined $r_{\text{sum};\beta}(X) := (\sum_{\mathbf{s} \in \mathcal{D}} |X(\mathbf{s})|^\beta)^{1/\beta}$. As X is on the standard Pareto scale, β can be selected as an estimate of the marginal tail index of Y , assuming that Y is heavy-tailed with $\mathbb{P}(Y(\mathbf{s}) > y) \sim cy^{-1/\beta}$, $c > 0$, as $y \rightarrow \infty$, for all $\mathbf{s} \in \mathcal{S}$; see [Section 5.2](#) for details.

A particular class of r -Pareto processes that we consider in this paper are the so-called Brown–Resnick r -Pareto processes; these are r -Pareto processes associated with Brown–Resnick max-stable processes, constructed as $\tilde{Z}(\mathbf{s}) = \max_{i \geq 1} \Gamma_i^{-1} \tilde{V}_i(\mathbf{s})$, $\mathbf{s} \in \mathcal{S}$, where $\{\Gamma_i\}_{i \geq 1}$ are the points of a unit rate Poisson point process and, independently, $\{\tilde{V}_i\}_{i \geq 1}$ are independent and identically distributed log-Gaussian processes. Specifically, each \tilde{V}_i is a copy of the process $\{\tilde{V}(\mathbf{s}), \mathbf{s} \in \mathcal{S}\}$ where $\tilde{V}(\mathbf{s}) = \exp\{\epsilon(\mathbf{s}) - \sigma^2(\mathbf{s})/2\}$, $\mathbf{s} \in \mathcal{S}$, and $\{\epsilon(\mathbf{s}), \mathbf{s} \in \mathcal{S}\}$ is a zero-mean Gaussian process with marginal variance $\sigma^2(\mathbf{s})$ at site \mathbf{s} and semivariogram $\gamma(\cdot, \cdot)$. The process V arising, as in (1), to construct the corresponding r -Pareto process counterpart has distribution characterized by $\mathbb{P}(V \in \cdot) = \mathbb{E}[r(\tilde{V}) \mathbf{1}\{\tilde{V}/r(\tilde{V}) \in \cdot\}]/\mathbb{E}[r(\tilde{V})]$, where $\mathbf{1}(\cdot)$ is the indicator function; see [Dombry et al. \(2024\)](#) for further details.

To measure the strength of extremal dependence between the process observed at two sites $\mathbf{s}_i, \mathbf{s}_j \in \mathcal{S}$, [de Fondeville and Davison \(2018\)](#) proposed using the conditional exceedance probability (CEP), defined as

$$\pi_{ij}(u, u') = \mathbb{P}[X(\mathbf{s}_j) \geq u' \mid \{X(\mathbf{s}_i) \geq u'\} \cap \{r(X/u) \geq 1\}], \quad (3)$$

for some high thresholds $u, u' > 1$. One can show that when both $u \rightarrow \infty$ and $u' \rightarrow \infty$ such that $u'/u \rightarrow \infty$, the CEP of the aforementioned Brown–Resnick r -Pareto process takes the limiting form $\pi_{ij} = \lim_{u, u' \rightarrow \infty} \pi_{ij}(u, u') = 2 \left[1 - \Phi \left\{ \sqrt{\gamma(\mathbf{s}_i, \mathbf{s}_j)/2} \right\} \right]$. We use this extremal dependence measure for both inference and model checking.

2.2 Modeling nonstationarity

The deep compositional spatial modeling approach of [Zammit-Mangion et al. \(2022\)](#) constructs a nonstationary covariance function using a composition of bijective warping functions, and we here extend it to the (non-Gaussian) extremal setting. Assume that r -exceedances of the process $\{X(\mathbf{s}), \mathbf{s} \in \mathcal{S}\}$ converge, when appropriately rescaled, to a Brown–Resnick r -Pareto process, characterized by a nonstationary semivariogram denoted here by $\gamma_{\mathcal{S}} : \mathcal{S} \times \mathcal{S} \rightarrow \mathbb{R}_+$. We construct a spatial deformation, also called “warping”, $\mathbf{f} : \mathcal{S} \rightarrow \mathcal{W}$, such that the process X is approximately stationary and isotropic on the warped domain \mathcal{W} . In other words, we assume that the semivariogram can be expressed as $\gamma_{\mathcal{S}}(\mathbf{s}_1, \mathbf{s}_2) = \gamma_{\mathcal{W}}(\|\mathbf{f}(\mathbf{s}_1) - \mathbf{f}(\mathbf{s}_2)\|)$ for $\mathbf{s}_1, \mathbf{s}_2 \in \mathcal{S}$, where $\gamma_{\mathcal{W}}(\cdot)$ is a semivariogram function that only depends on the distance $\|\mathbf{f}(\mathbf{s}_1) - \mathbf{f}(\mathbf{s}_2)\|$ between $\mathbf{f}(\mathbf{s}_1), \mathbf{f}(\mathbf{s}_2) \in \mathcal{W}$. In this paper, we take the (common) power variogram $\gamma_{\mathcal{W}}(\mathbf{s}_1, \mathbf{s}_2) = (\|\mathbf{s}_1 - \mathbf{s}_2\|/\varphi)^\kappa$, with range parameter $\varphi > 0$ and smoothness parameter $\kappa \in (0, 2)$, and let $\boldsymbol{\psi} = (\varphi, \kappa)'$. Therefore, on the original space, the semivariogram $\gamma_{\mathcal{S}}$ is parametrized by both the parameter vector $\boldsymbol{\psi}$ and the warping function \mathbf{f} and has the form $\gamma_{\mathcal{S}}(\mathbf{s}_1, \mathbf{s}_2) := \gamma_{\mathcal{S}}(\mathbf{s}_1, \mathbf{s}_2; \boldsymbol{\psi}, \mathbf{f}) = (\|\mathbf{f}(\mathbf{s}_1) - \mathbf{f}(\mathbf{s}_2)\|/\varphi)^\kappa$.

Constructing a flexible family of bijective warpings that can be estimated efficiently is challenging. Following [Zammit-Mangion et al. \(2022\)](#), we build the warping function $\mathbf{f}(\cdot)$ as a composition of n warping units, i.e., $\mathbf{f}(\cdot) = \mathbf{f}_n \circ \mathbf{f}_{n-1} \circ \cdots \circ \mathbf{f}_1(\cdot)$, where each $\mathbf{f}_i(\cdot)$ is taken to be a simple bijective function. Each warping unit $\mathbf{f}_i : \mathcal{W}_{i-1} \rightarrow \mathcal{W}_i$ maps $\mathcal{W}_{i-1} \subset \mathbb{R}^K$ to $\mathcal{W}_i \subset \mathbb{R}^K$, where $\mathcal{W}_0 := \mathcal{S}$ is the original spatial domain, and $\mathcal{W}_n := \mathcal{W}$ denotes the target warped space \mathcal{W} . For all $i = 1, \dots, n$, we parametrize each warping unit $\mathbf{f}_i(\cdot)$ in terms of basis functions $\phi_i(\cdot; \boldsymbol{\Theta}_i)$, which depend on a parameter vector $\boldsymbol{\Theta}_i$ to be estimated, and a weight matrix \mathbf{W}_i also to be estimated. [Zammit-Mangion et al. \(2022\)](#) proposed three types of warping units, which we also consider in this paper and review below: axial warping, radial basis function, and Möbius transformation units.

Axial Warping (AW) Unit An AW unit is a nonlinear mapping of one input dimension of the spatial ordinate $\mathbf{s} \in \mathcal{S}$. The map is constrained to be strictly monotonic, and hence bijective. For some fixed $k = 1, \dots, K$, the AW unit, $\mathbf{f}_i(\cdot) = \{f_{i1}(\cdot), \dots, f_{iK}(\cdot)\}$, warps the

k -th input dimension and is defined such that $f_{ik}(\mathbf{s}) = \mathbf{W}_i^{(k)} \boldsymbol{\phi}_i(\mathbf{s}; \boldsymbol{\Theta}_i)$ and $f_{ik'}(\mathbf{s}) = s_{k'}$ for $k' \neq k$ (that is, only the k -th component of \mathbf{s} is affected), where $\boldsymbol{\phi}_i(\cdot) = (\phi_{i1}(\cdot), \dots, \phi_{im_i}(\cdot))'$ comprises m_i basis functions with $\phi_{i1}(\mathbf{s}) = s_k$ and $\phi_{ij}(\mathbf{s}; \boldsymbol{\theta}_{ij}) = [1 + \exp\{-\theta_{ij1}(s_k - \theta_{ij2})\}]^{-1}$, $\boldsymbol{\theta}_{ij} = (\theta_{ij1}, \theta_{ij2})'$, for $j = 2, \dots, m_i$. Weights $\mathbf{W}_i^{(k)} = (w_{i1}, \dots, w_{im_i})$ are required to be non-negative to ensure the bijectivity of $\mathbf{f}_i(\cdot)$, and $\boldsymbol{\Theta}_i = (\theta_{i21}, \theta_{i22}, \dots, \theta_{im_i1}, \theta_{im_i2})'$ are fixed to produce smooth warping functions over the entire domain of the k -th input dimension of \mathcal{W}_{i-1} . Among all m_i basis functions, the first basis function $\phi_{i1}(\cdot)$ controls linear scaling of the k -th input dimension, and the remaining basis functions, $\phi_{i2}(\cdot), \dots, \phi_{im_i}(\cdot)$, control its nonlinear scaling with sigmoid functions.

Radial Basis Function (RBF) Unit The RBF unit provides a localized expansion or contraction of the space around a centroid. An RBF unit $\mathbf{f}_i(\cdot)$, for $\mathbf{s} \in \mathcal{W}_{i-1}$, is defined as

$$\mathbf{f}_i(\mathbf{s}) = \mathbf{s} + w_i (\mathbf{s} - \mathbf{c}_i) \exp\{-b_i \|\mathbf{s} - \mathbf{c}_i\|^2\},$$

where $b_i > 0$ is a learnable rate parameter, $\mathbf{c}_i = (c_{i1}, \dots, c_{iK})' \in \mathcal{W}_{i-1}$ denotes the warping centroid, and w_i controls the intensity of stretching ($w_i > 0$) or shrinking ($w_i < 0$); when $w_i = 0$, $\mathbf{f}_i(\cdot)$ is the identity function. For $K = 2$, $\mathbf{f}_i(\cdot)$ can be equivalently expressed as $\mathbf{f}_i(\cdot) = \mathbf{W}_i \boldsymbol{\phi}_i(\cdot; \boldsymbol{\Theta}_i)$ with

$$\boldsymbol{\phi}_i(\cdot) = (\phi_{i1}(\cdot), \phi_{i2}(\cdot), \phi_{i3}(\cdot), \phi_{i4}(\cdot))' \text{ with } \begin{cases} \phi_{i1}(\mathbf{s}) = s_1 \\ \phi_{i2}(\mathbf{s}) = s_2 \\ \phi_{i3}(\mathbf{s}; \boldsymbol{\Theta}_i) = (s_1 - c_{i1}) \exp(-b_i \|\mathbf{s} - \mathbf{c}_i\|^2) \\ \phi_{i4}(\mathbf{s}; \boldsymbol{\Theta}_i) = (s_2 - c_{i2}) \exp(-b_i \|\mathbf{s} - \mathbf{c}_i\|^2) \end{cases};$$

here $\boldsymbol{\Theta}_i = (\mathbf{c}_i', b_i)'$ and $\mathbf{W}_i = [\mathbf{I}_2 \ w_i \mathbf{I}_2]$, with \mathbf{I}_2 the 2×2 identity matrix. The weight w_i must satisfy $-1 < w_i < \exp(3/2)/2$ to enforce injectivity (Perrin and Monestiez, 1999).

In order to simplify computations, Zammit-Mangion et al. (2022) utilized the single-resolution RBF unit, which is parameterized by a resolution $l \in \mathbb{N}_+$; we denote this by SR-RBF(l). The SR-RBF(l) unit is formed as a composition of RBF units, with centroids

\mathbf{c}_i fixed on a $3^l \times 3^l$ grid in \mathcal{W}_{i-1} and b_i set to $b_i = 2(3^l - 1)^2$ for all layers. As a result, the SR-RBF(l) unit has 3^{2l} layers and only one weight, w_i , needs to be estimated per layer.

Möbius Transformation (MT) Unit The Möbius transformation is a bijective, conformal map from the Riemann sphere onto itself; it rotates and moves the sphere to a new location and orientation in space, and then performs stereographic projection back to the plane. Thus, it can only be applied when $\mathcal{S} \subseteq \mathbb{R}^2$, i.e., $K = 2$; we hereafter assume this to hold. The MT unit is defined through the function

$$\phi_i(\mathbf{s}; \boldsymbol{\Theta}_i) = \frac{a_1 z(\mathbf{s}) + a_2}{a_3 z(\mathbf{s}) + a_4},$$

where $z(\mathbf{s}) = s_1 + s_2\sqrt{-1}$, $\mathbf{a} \in \mathbb{C}^4$, $\boldsymbol{\Theta}_i = (a_1, \dots, a_4)'$. This warping unit contains eight unknown parameters (the real and imaginary components of a_1, \dots, a_4) and all weights \mathbf{W}_i are fixed to one. Finally, $f_{i1}(\mathbf{s}) = \text{Re}(\phi_i(\mathbf{s}; \boldsymbol{\Theta}_i))$ and $f_{i2}(\mathbf{s}) = \text{Im}(\phi_i(\mathbf{s}; \boldsymbol{\Theta}_i))$, $\mathbf{s} \in \mathcal{W}_{i-1}$, where $\text{Re}(\cdot)$ and $\text{Im}(\cdot)$ return the real and imaginary components, respectively, of their arguments. Note that Möbius transformations form a group under composition, so it is unnecessary to apply successive MT units in the compositional warping.

3 Inference

3.1 Model fitting by loss minimization

Suppose that $\mathbf{x} = \{x(\mathbf{s}_i)\}_{i=1}^D \in \mathbb{R}_+^D$ is a realization of the normalized process $X = \{X(\mathbf{s}), \mathbf{s} \in \mathcal{S}\}$ (with standard Pareto margins) at D locations in $\mathcal{D}_0 = \{\mathbf{s}_1, \dots, \mathbf{s}_D\} \subset \mathcal{S}$, and assume that the rescaled r -exceedances of X , i.e., X/u given $r(X) > u$, converge weakly to a nonstationary r -Pareto process Z as u goes to infinity. In the sequel, we only consider risk functionals that involve variables observed at locations within the finite set \mathcal{D}_0 and thus, by abuse of notation, we write $r(\mathbf{x})$ to denote the risk functional evaluated at the realization \mathbf{x} . An approximate realization of the limit process Z at the locations in \mathcal{D}_0 is then given by $\mathbf{z} = \mathbf{x}/u$ such that $r(\mathbf{x}) > u$, for some high threshold $u > 1$. In practice, for N independent replicates $\{\mathbf{x}_t\}_{t=1}^N$, the threshold u is taken to be a high empirical

quantile of $\{r(\mathbf{x}_t)\}_{t=1}^N$. The (approximate) negative log-likelihood function associated with the limiting r -Pareto process may thus be written as

$$\ell(\boldsymbol{\psi}, \mathbf{f}) = - \sum_{t=1}^N \mathbb{1} \left\{ r \left(\frac{\mathbf{x}_t}{u} \right) \geq 1 \right\} \log \lambda_r \left(\frac{\mathbf{x}_t}{u}; \boldsymbol{\psi}, \mathbf{f} \right), \quad (4)$$

where $\lambda_r(\mathbf{z}; \boldsymbol{\psi}, \mathbf{f})$ denotes the probability density function of the r -Pareto process, which is of the form $\lambda_r(\mathbf{z}; \boldsymbol{\psi}, \mathbf{f}) := \lambda(\mathbf{z}; \boldsymbol{\psi}, \mathbf{f}) / \Lambda(\mathcal{A}_r; \boldsymbol{\psi}, \mathbf{f})$ defined over the support $\mathcal{A}_r := \{\mathbf{z} \in \mathbb{R}_+^D : r(\mathbf{z}) \geq 1\}$, and with $\boldsymbol{\psi}$ and \mathbf{f} the vector of extremal dependence parameters and warping function, respectively, to be estimated; here, $\lambda(\mathbf{z}; \boldsymbol{\psi}, \mathbf{f})$ is a suitable parametric intensity function and $\Lambda(\mathcal{A}_r; \boldsymbol{\psi}, \mathbf{f})$ is a normalizing factor given by integrating $\lambda(\mathbf{z}; \boldsymbol{\psi}, \mathbf{f})$ over the exceedance region \mathcal{A}_r , i.e., $\Lambda(\mathcal{A}_r; \boldsymbol{\psi}, \mathbf{f}) := \int_{\mathcal{A}_r} \lambda(\mathbf{z}; \boldsymbol{\psi}, \mathbf{f}) d\mathbf{z}$. Note that $\lambda_r(\mathbf{z}; \boldsymbol{\psi}, \mathbf{f})$ is dependent on the chosen risk functional $r(\cdot)$. Specifically, when Z is the Brown–Resnick r -Pareto process defined in terms of log-Gaussian functions with semivariogram $\gamma_{\mathcal{S}}(\cdot, \cdot; \boldsymbol{\psi}, \mathbf{f})$, the intensity function is (Engelke et al., 2015)

$$\lambda(\mathbf{z}; \boldsymbol{\psi}, \mathbf{f}) = \frac{|\boldsymbol{\Sigma}_{\boldsymbol{\psi}, \mathbf{f}}|^{-1/2}}{z_1^2 z_2 \cdots z_D (2\pi)^{(D-1)/2}} \exp \left(-\frac{1}{2} \tilde{\mathbf{z}}^T \boldsymbol{\Sigma}_{\boldsymbol{\psi}, \mathbf{f}}^{-1} \tilde{\mathbf{z}} \right), \quad (5)$$

with $(D-1)$ -dimensional vector $\tilde{\mathbf{z}} = \{\log(z_i/z_1) + \gamma_{i,1}\}_{i=2}^D$, and $(D-1)$ -dimensional square matrix $\boldsymbol{\Sigma}_{\boldsymbol{\psi}, \mathbf{f}} = (\gamma_{i,1} + \gamma_{j,1} - \gamma_{i,j})_{2 \leq i,j \leq D}$ for $z_i = z(\mathbf{s}_i)$ and $\gamma_{i,j} = \gamma_{\mathcal{S}}(\mathbf{s}_i, \mathbf{s}_j; \boldsymbol{\psi}, \mathbf{f})$, $i, j = 1, \dots, D$. The computational bottleneck when minimizing (4) comes from the evaluation of the multivariate D -dimensional integral $\Lambda(\mathcal{A}_r; \boldsymbol{\psi}, \mathbf{f})$ for a general risk functional $r(\cdot)$, which makes full likelihood inference for r -Pareto processes intractable when D is large. Furthermore, Wadsworth and Tawn (2014) and de Fondeville and Davison (2018) developed a censored likelihood based on (4) that incorporates both fully observed extreme values and partially-observed extreme values, where any component z_i lying below a marginal threshold is treated as censored; evaluating a censored likelihood further requires multiple partial integrals of the density $\lambda_r(\mathbf{z}; \boldsymbol{\psi}, \mathbf{f})$. Although general expressions exist for censored likelihood contributions when considering the Brown–Resnick r -Pareto process, they involve multivariate Gaussian distribution functions that are costly to evaluate in high dimensions. de Fondeville and Davison (2018) advocated quasi-Monte Carlo methods to accelerate their

evaluation, but these remain intensive when estimating model parameters with hundreds of locations. We here make use of the censored likelihood to assess model performance in subsequent studies (see Sections 4 and 5), but adopt a more computationally efficient loss function for estimation; for brevity, we do not detail the censored likelihood and instead direct the reader to [de Fondeville and Davison \(2018\)](#) for full mathematical details.

Inference for the deep compositional r -Pareto process X thus involves jointly optimizing the dependence parameters $\boldsymbol{\psi}$ along with the warping function weights and parameters, denoted by $\mathbf{W} = \{\mathbf{W}_1, \dots, \mathbf{W}_n\}$ and $\boldsymbol{\Theta} = \{\boldsymbol{\Theta}_1, \dots, \boldsymbol{\Theta}_n\}$, with respect to a chosen loss function. Each warping unit $\mathbf{f}_i(\cdot)$, parameterized by \mathbf{W}_i and $\boldsymbol{\Theta}_i$, maps sampling locations $\mathcal{D}_{i-1} \subset \mathcal{W}_{i-1}$ to $\mathcal{D}_i \subset \mathcal{W}_i$, $i = 1, \dots, n$, where $\mathcal{D}_0 \subset \mathcal{S}$ denotes the original sampling locations. All location sets, $\mathcal{D}_0, \dots, \mathcal{D}_n$, are rescaled to lie in $[-0.5, 0.5]^2$ to ensure numerical stability of model training. Only the relative distance between locations in the warped space affects the extremal dependence structure; rescaling may influence the range parameter φ , but preserves the underlying geometry of the warped space.

We consider two loss functions for fitting deep compositional r -Pareto processes: i) a weighted square error loss on conditional exceedance probabilities with data-adaptive weights, which is computationally efficient and only uses information from pairs of sites; and ii) the gradient score matching approach of [de Fondeville and Davison \(2018\)](#), which exploits information contained in the entire multivariate vector.

Weighted least squares An intuitive approach for inference is to minimize the (weighted) square error between the theoretical model-based CEPs, i.e., $\pi_{ij}(u, u'; \boldsymbol{\psi}, \mathbf{f})$ in (3), determined by the dependence parameters $\boldsymbol{\psi}$ and warping \mathbf{f} , and their corresponding empirical counterparts. We pre-estimate the empirical counterparts, denoted as $\hat{\pi}_{ij}(u, u')$ for sites \mathbf{s}_i and \mathbf{s}_j , using the formula:

$$\hat{\pi}_{ij}(u, u') = \frac{\sum_{t=1}^N \mathbb{1}\{x_t(\mathbf{s}_i) \geq u', x_t(\mathbf{s}_j) \geq u', r(\mathbf{x}_t) \geq u\}}{\frac{1}{2} \left[\sum_{t=1}^N \mathbb{1}\{x_t(\mathbf{s}_i) \geq u', r(\mathbf{x}_t) \geq u\} + \sum_{t=1}^N \mathbb{1}\{x_t(\mathbf{s}_j) \geq u', r(\mathbf{x}_t) \geq u\} \right]},$$

where the denominator achieves symmetry, i.e., $\hat{\pi}_{ij}(u, u') = \hat{\pi}_{ji}(u, u')$. In practice, u is chosen as described above, while u' , a common marginal threshold, is chosen to be some

(common) high empirical marginal quantile of $\{x_t(\mathbf{s}), \mathbf{s} \in \mathcal{D}_0\}_{t=1}^N$. We write the (weighted) least squares loss function ℓ_{WLS} as

$$\ell_{\text{WLS}}(\boldsymbol{\psi}, \mathbf{f}) = \sum_{1 \leq i < j \leq D} \check{w}_{ij} \{\pi_{ij}(u, u'; \boldsymbol{\psi}, \mathbf{f}) - \hat{\pi}_{ij}(u, u')\}^2, \quad (6)$$

with weights $\check{w}_{ij} \geq 0, i, j = 1, \dots, D$. The estimated dependence parameter vector $\hat{\boldsymbol{\psi}}_{\text{WLS}}$ and warping $\hat{\mathbf{f}}_{\text{WLS}}$, based on the weights $\hat{\mathbf{W}}_{\text{WLS}}$ and parameters $\hat{\boldsymbol{\Theta}}_{\text{WLS}}$, are obtained by minimizing $\ell_{\text{WLS}}(\boldsymbol{\psi}, \mathbf{f})$. For the choice of weights in (6), a natural approach is to assign more weight \check{w}_{ij} to closer location pairs and to downweight distant ones, but it may not be appropriate for nonstationary models. [Huser and Genton \(2016\)](#) indicate that observation pairs with stronger extremal dependence contribute more to the fit of stationary models; based on this observation, we choose a data-driven scheme to assign more weight to pairs $(\mathbf{s}_i, \mathbf{s}_j)$ with stronger extremal dependence, where two simple choices include i) $\check{w}_{ij} = \hat{\pi}_{ij}(u, u') \in [0, 1]$ or ii) $\check{w}_{ij} = 1/\{2 - \hat{\pi}_{ij}(u, u')\} \in [1/2, 1]$; we find the latter preferable in our experiments, as estimates of $\hat{\pi}_{ij}(u, u')$ often vanish when u' is large, such that using the former may eliminate too many pairs that are weakly dependent in the tail, leading to information loss.

Gradient score matching [de Fondeville and Davison \(2018\)](#) studied a computationally efficient inference method for Brown–Resnick r -Pareto processes that utilizes gradient score matching. The gradient score matching (GSM) method was developed by [Hyvärinen and Dayan \(2005\)](#) to estimate models for which the density cannot be easily normalized. The pivotal idea is that the normalizing constant in (4), i.e., the multivariate integral $\Lambda(\mathcal{A}_r; \boldsymbol{\psi}, \mathbf{f})$, disappears when taking the gradient of the log-densities, i.e., $\nabla_{\mathbf{z}} \log \lambda_r(\mathbf{z}; \boldsymbol{\psi}, \mathbf{f}) = \nabla_{\mathbf{z}} \log \lambda(\mathbf{z}; \boldsymbol{\psi}, \mathbf{f})$, which eliminates the need to compute the multivariate integral $\Lambda(\mathcal{A}_r; \boldsymbol{\psi}, \mathbf{f})$. Hence, [de Fondeville and Davison \(2018\)](#) proposed minimizing a divergence measure, defined by the expected (weighted) squared distance between the

model score function and the true data generating score function, i.e.,

$$\delta(\mathbf{z}; \boldsymbol{\psi}, \mathbf{f}) = \int_{\mathcal{A}_r} \|\nabla_{\mathbf{z}} \log \lambda(\mathbf{z}; \boldsymbol{\psi}, \mathbf{f}) \otimes \tilde{\mathbf{w}}(\mathbf{z}) - \nabla_{\mathbf{z}} \log \lambda(\mathbf{z}; \boldsymbol{\psi}_0, \mathbf{f}_0) \otimes \tilde{\mathbf{w}}(\mathbf{z})\|_2^2 \lambda(\mathbf{z}; \boldsymbol{\psi}_0, \mathbf{f}_0) d\mathbf{z}, \quad (7)$$

where $\boldsymbol{\psi}_0$ and \mathbf{f}_0 denote the true dependence parameters and true warping, respectively, $\tilde{\mathbf{w}} : \mathcal{A}_r \rightarrow \mathbb{R}_+^D$ is a positive weight function, and \otimes denotes the componentwise product. Under some boundary and differentiability conditions imposed on the weight function, [de Fondeville and Davison \(2018\)](#) showed that the empirical version of (7) is, up to an additive constant, equal to

$$\begin{aligned} \hat{\delta}(\mathbf{z}; \boldsymbol{\psi}, \mathbf{f}) = \sum_{i=1}^D & \left(2\tilde{w}_i(\mathbf{z}) \frac{\partial \tilde{w}_i(\mathbf{z})}{\partial z_i} \frac{\partial \log \lambda(\mathbf{z}; \boldsymbol{\psi}, \mathbf{f})}{\partial z_i} \right. \\ & \left. + \tilde{w}_i^2(\mathbf{z}) \left[\frac{\partial^2 \log \lambda(\mathbf{z}; \boldsymbol{\psi}, \mathbf{f})}{\partial z_i^2} + \frac{1}{2} \left\{ \frac{\partial \log \lambda(\mathbf{z}; \boldsymbol{\psi}, \mathbf{f})}{\partial z_i} \right\}^2 \right] \right), \end{aligned}$$

where $z_i \equiv z(\mathbf{s}_i)$ and $\tilde{w}_i(\cdot)$ is the i -th component of $\tilde{\mathbf{w}}(\cdot)$. To further adapt to extremes, $\tilde{\mathbf{w}}(\cdot)$ can be designed to penalize low r -exceedances when $r(\mathbf{z})$ is close to u with low weight. [de Fondeville and Davison \(2018\)](#) proposed two weight functions. While they advocated one which is designed to mimic marginal censoring by downweighting components of \mathbf{z} near u , in practice we found that such a design has the tendency to assign zero weight to too many low components; this removes substantial information, which leads to estimation difficulties in the presence of high-dimensional data. Based on our experiments, we thus use the alternative weight function, defined as $\tilde{w}_i(\mathbf{z}) = z_i[1 - \exp\{1 - r(\mathbf{z})\}]$, $i = 1, \dots, D$, as it is simpler and performs better in our setting. The computational complexity of the loss function is now determined only by the inversion of the $(D - 1)$ -dimensional matrix $\boldsymbol{\Sigma}_{\boldsymbol{\psi}, \mathbf{f}}$ in (5); the gradient score matching loss $\ell_{\text{GSM}}(\boldsymbol{\psi}, \mathbf{f})$ is

$$\ell_{\text{GSM}}(\boldsymbol{\psi}, \mathbf{f}) = \sum_{t=1}^N \mathbb{1} \left\{ r \left(\frac{\mathbf{x}_t}{u} \right) \geq 1 \right\} \hat{\delta} \left(\frac{\mathbf{x}_t}{u}; \boldsymbol{\psi}, \mathbf{f} \right). \quad (8)$$

The estimated dependence parameter vector $\hat{\boldsymbol{\psi}}_{\text{GSM}}$ and warping $\hat{\mathbf{f}}_{\text{GSM}}$, based on the weights $\hat{\mathbf{W}}_{\text{GSM}}$ and parameters $\hat{\boldsymbol{\Theta}}_{\text{GSM}}$, are obtained by minimizing $\ell_{\text{GSM}}(\boldsymbol{\psi}, \mathbf{f})$. Under certain regu-

larity conditions and fixed warping, $\hat{\psi}_{\text{GSM}}$ can be shown to be consistent and asymptotically normal; see [Hyvärinen and Dayan \(2005\)](#) and [Hyvärinen \(2007\)](#) for details.

An advantage of the gradient score matching method is that it exploits the full intensity $\lambda(\cdot)$, and hence information from the entire multivariate vector, rather than just information contained in pairwise extremal dependence estimates (as with the CEP in (6)). As it is based on the (unnormalized) likelihood function, we can expect it to be more efficient than a moment-based approach (like least squares) based on CEPs. However, the gradient score matching approach is potentially less robust to outliers and model misspecification, and has a heavier computational burden than the weighted least squares method.

3.2 Regularization techniques

To prevent overfitting when the warping $\mathbf{f}(\cdot)$ includes “overly-flexible” units, we add to the loss function a regularization term penalizing their weights. In our implementation, we only penalize the weights of SR-RBF(l) units with $l \geq 2$ (recall Section 2.2), when such units are included in the model’s architecture. The resulting regularized loss function, denoted $\tilde{\ell}(\cdot)$, modifies the original loss $\ell(\cdot)$ —either $\ell_{\text{WLS}}(\cdot)$ in (6) or $\ell_{\text{GSM}}(\cdot)$ in (8)—by adding a penalty equal to the sum of squared weights from the SR-RBF(l) unit, i.e.,

$$\tilde{\ell}(\cdot) = \ell(\cdot) + \alpha \sum_{i=1}^{n_l} w_i^2, \quad (9)$$

where $\alpha > 0$ is a penalty parameter, n_l denotes the depth of the SR-RBF(l) unit, and $w_i, i = 1, \dots, n_l$, denotes the weight of each layer. The coefficient α can be optimized via a grid search and, in unreported experiments related to our simulation study and data application, we found that setting $\alpha = 1$ generally performs satisfactorily. Models with complex architectures comprising the SR-RBF(l) unit with $l \geq 2$ are thus penalized by the above ridge regularizer, and we set $\tilde{\ell}(\cdot) = \ell(\cdot)$ if these units are not included. An alternative approach to prevent overfitting could exploit cross-validation, which examines the model performance by assessing the loss over a carefully chosen out-of-sample validation set; see, e.g., [Wang et al. \(2023\)](#). Better performance over the validation locations indicates

better generality of the estimated model. Nevertheless, we found that this method can be very sensitive to the choice of validation locations, especially in a nonstationary setting where estimating the spatial warping is of interest, and it may result in underestimating the warping complexity; hence, we instead utilize our simple regularization technique with $\alpha = 1$ fixed to enhance model generalization.

3.3 Implementation details

We minimize the regularized loss function $\tilde{\ell}(\cdot)$ in (9) using the Adam algorithm (Kingma and Ba, 2015), which adaptively scales each parameter’s learning rate by keeping exponentially decaying averages of past gradients (first moments) and squared gradients (second moments). Only one of $\boldsymbol{\psi}$, $\boldsymbol{\Theta}$, and \boldsymbol{W} is optimized at each step of the optimization procedure. Compared to vanilla stochastic gradient descent, Adam enjoys a number of merits, e.g., it converges faster and better handles noisy gradients, and hence, Adam is preferable for complex models and tasks where training is computationally expensive.

In contrast with the Gaussian case, providing suitable theoretical uncertainty quantification for extremal dependence estimates is challenging. We jointly assess the uncertainty of both dependence parameters, $\hat{\boldsymbol{\psi}}$, and the warping, $\hat{\boldsymbol{f}}(\cdot)$, as well as pairwise CEP estimates over the fitted warped space through the use of a nonparametric bootstrap. Whilst the asymptotic normality of $\hat{\boldsymbol{\psi}}$ and the multivariate Delta method may provide another approach to achieve this, they are unable to account for the uncertainty in the estimation of the warping. Theoretical results for the asymptotic behaviour of $\hat{\boldsymbol{\psi}}$ that account for the highly flexible, highly parametrized warping $\boldsymbol{f}(\cdot)$ are beyond the scope of this work.

The proposed model is implemented using the `Tensorflow` interface in R, specifically with `Tensorflow` version 2.11.0 and Python version 3.7.11.

Table 1: Architectures of deep compositional r -Pareto processes. The depth n of each compositional model is also provided.

Architecture	n	AW	SR-RBF(1)	SR-RBF(2)	MT
0	0				
1	12	✓	✓		✓
2	93	✓	✓	✓	✓
3	11	✓	✓		
4	92	✓	✓	✓	

4 Simulation study

4.1 Overview

We illustrate the efficacy of our proposed model by simulating r -Pareto processes over a pre-defined warped space and estimating their nonstationary extremal dependence structure. We use a true compositional warping $\mathbf{f}(\cdot)$ consisting of three warping units (see Section 2.2), where four different architectures (see Table 1) of the deep model are considered. For the choice of architectures, we start with two general scenarios comprising all three types of warping units introduced in Section 2.2: axial warping (AW) units, single resolution radial basis functions (denoted as SR-RBF(l) with resolution $l = 1$ or $l = 2$), and a Möbius transformation (MT) unit. Specifically, Architecture 1 corresponds to a 12-layered compositional warping $\mathbf{f}(\cdot)$, where $\mathbf{f}_1(\cdot)$ and $\mathbf{f}_2(\cdot)$ are axial warping units (one for each spatial dimension), $\mathbf{f}_3(\cdot), \dots, \mathbf{f}_{11}(\cdot)$ comprise a 9-layered SR-RBF(1) unit, and $\mathbf{f}_{12}(\cdot)$ is a MT unit. Architecture 2 has an additional 81-layered SR-RBF(2) unit after the SR-RBF(1) unit in Architecture 1. More complicated warping units, e.g., a 729-layered SR-RBF(3) unit, could also be used, but here we stop at resolution $l = 2$ due to the additional computational burden and to reduce the risk of overfitting. In spite of this, we still find that our models are sufficiently flexible, and capture well the extremal dependence of the data in both our simulation study and subsequent data application. Architectures 3 and 4 are the same as Architectures 1 and 2, respectively, but without the MT unit. Models with Architecture k are hereafter termed as “nonstationary model k ”, $k = 1, \dots, 4$. Architecture 0 denotes the “null” stationary and isotropic model, where no deformation is performed.

In our simulation study, the original spatial locations \mathcal{D}_0 are chosen to be on a regular 101×101 grid within the unit square $[-0.5, 0.5]^2$, and $\mathcal{D}_n = \mathbf{f}(\mathcal{D}_0)$ is created by randomly generating the weights $\mathbf{W} = \{\mathbf{W}_1, \dots, \mathbf{W}_n\}$ and parameters $\boldsymbol{\Theta} = \{\boldsymbol{\Theta}_1, \dots, \boldsymbol{\Theta}_n\}$ of the compositional model. Each architecture has its own “true” warped space \mathcal{W} , as shown in Figure 1 for Architecture 3. To facilitate comparisons, we maintain the same weights and parameters for all warping units, i.e., AW, SR-RBF(1), SR-RBF(2), and MT units in each architecture, which enables warped spaces generated using these four architectures to share some similarities and allows us to study the impact of each warping unit. To assess the effect of architecture misspecification, which is likely to occur in real data applications, we perform a factorial simulation experiment. Specifically, we generate, for each architecture, its own true warped space. Then, we simulate a Brown–Resnick r -Pareto process with power semivariogram over each of the four “true” warped domains, i.e., we use the semivariogram $\gamma_{\mathcal{S}}(\mathbf{s}_1, \mathbf{s}_2; \boldsymbol{\psi}, \mathbf{f}) = (\|\mathbf{f}(\mathbf{s}_1) - \mathbf{f}(\mathbf{s}_2)\|/\varphi)^\kappa$, $\mathbf{s}_1, \mathbf{s}_2 \in \mathcal{S}$ (with range parameter $\varphi = 0.2$ and smoothness parameter $\kappa = 1$). Finally, we fit the deep compositional r -Pareto processes, with each of the four different architectures, to each of the four datasets; this results in a total of 16 models to fit. Figure 1 provides the true warped domain for Architecture 3; see Figures S1, S2, and S3 in the Supplementary Material for the true warped domains generated using Architectures 1, 2, and 4.

For each true warped domain \mathcal{W} , we generate $N = 5000$ replicates of a nonstationary r -Pareto process Z , denoted as $\{\mathbf{z}_t\}_{t=1}^N$, with three considered risk functionals:

$$r_{\text{site}}(Z) = Z(\mathbf{s}_0), \quad r_{\text{max}}(Z) = \max_{\mathbf{s} \in \mathcal{D}_0} Z(\mathbf{s}), \quad \text{and} \quad r_{\text{sum}}(Z) = \sum_{\mathbf{s} \in \mathcal{D}_0} Z(\mathbf{s}), \quad (10)$$

where $\mathcal{D}_0 = \{\mathbf{s}_1, \dots, \mathbf{s}_D\} \in \mathcal{S}$. As $r_{\text{max}}(\cdot)$ is not differentiable, an approximation $r_{\text{max}}(Z) \approx \{\sum_{\mathbf{s} \in \mathcal{D}_0} Z(\mathbf{s})^{20}\}^{1/20}$ is used instead. Direct simulation of r -Pareto processes is only available for some risk functionals, e.g., $r_{\text{site}}(\cdot)$, but simulation is feasible for a general functional $r(\cdot)$ using the rejection sampling method of [de Fondeville and Davison \(2018\)](#) and [Dombry et al. \(2024\)](#). We implement the simulation of such processes in **R**, where parallel computing is exploited to relieve the low acceptance rate problem for some scenarios. The threshold u is set to the empirical 95% quantile of the risks $\{r(\mathbf{z}_1), \dots, r(\mathbf{z}_N)\}$, giving rise to $N_u = 250$

r -exceedances, and u' is set to the empirical 95% marginal quantile. Among the $D = 101^2$ locations, $D_{\text{train}} = 500$ and $D_{\text{test}} = 100$ locations are randomly chosen as the training and test locations, respectively; we use the former to fit the model and the latter to assess out-of-sample accuracy of the estimated nonstationary extremal dependence structure. As the risk functional used in model fitting differs from the risk functional used to simulate the data, fitting r -Pareto process models inevitably introduces some risk-based misspecification, especially when using the max-functional. However, our subsequent simulation study shows that, for models incorporating the max-functional, this risk-based misspecification has a negligible effect on the model fits and warped space estimates. To quantify model performance, we compute the censored likelihood over the test locations, evaluated at the estimated dependence parameters, using the `mvPot` package (de Fondeville and Davison, 2018).

4.2 Results

We illustrate the efficacy of the proposed modeling approach by investigating the extremal dependence structure relative to three reference sites (see, e.g., Figure 1), where an obvious nonstationary extremal dependence pattern can be observed. For r -Pareto processes generated from each architecture, we first fit the deep compositional r -Pareto model using the true risk functional with four different architectures. In all four scenarios, both the gradient score matching (GSM) and weighted least squares (WLS) inference methods, described in Section 3.1, are tested. Using the estimated weights $\hat{\mathbf{W}}$ and parameters $\hat{\boldsymbol{\Theta}}$ of the compositional model, we visualize the estimated warped spaces in Figure 1 for Architecture 3, and Figures S1, S2, and S3 in the Supplementary Material for Architectures 1, 2, and 4, respectively, where the data are generated with the risk functional $r_{\max}(\cdot)$.

When the data are generated using Architecture 3 (AW + SR-RBF(1)), Figure 1 shows that, as expected, the model with the “correct” architecture, i.e., nonstationary model 3, provides the best estimate of the warped space. We also observe that nonstationary model 1 with a similar architecture (with only an additional MT unit) can also estimate the true warped space well. Table 2, showing the quantification of model fit accuracy using the

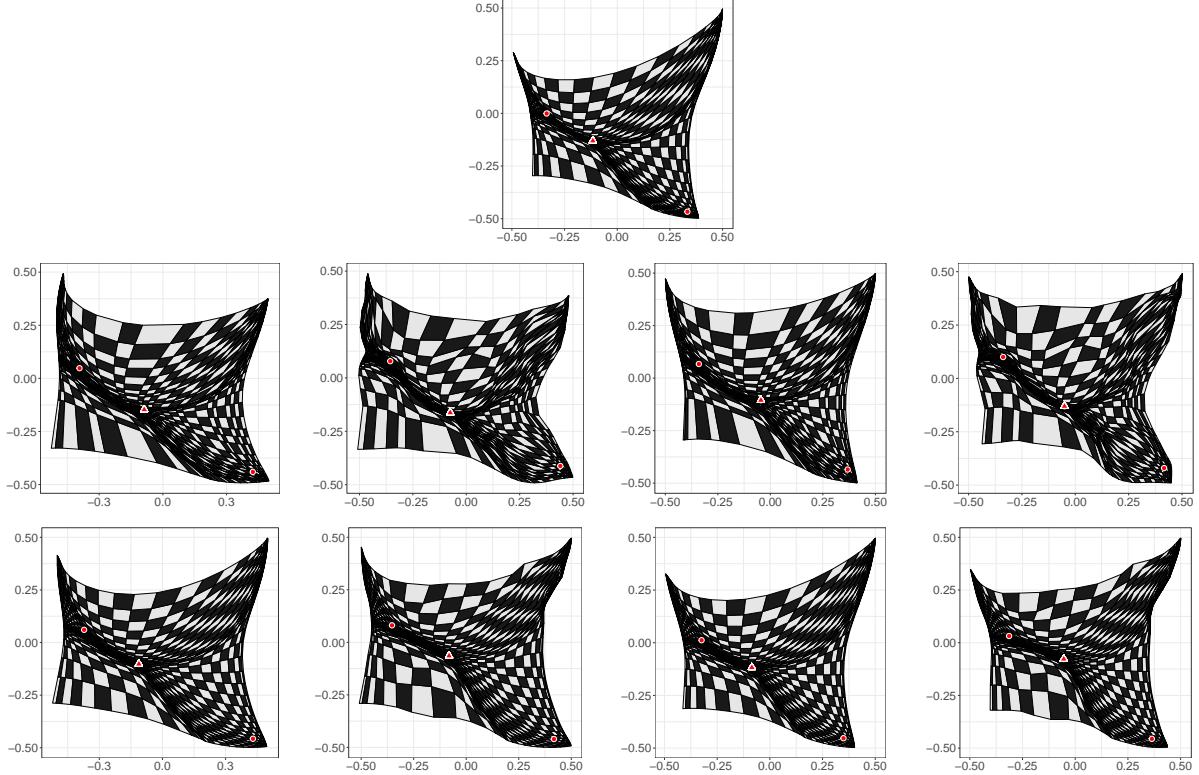


Figure 1: Top row: true warped domain \mathcal{W} generated using Architecture 3. Middle and bottom rows: estimated warped space $\hat{\mathcal{W}}$ using nonstationary models 1–4 (column 1–4) with WLS and GSM inference methods, respectively. The data are generated with the risk functional $r_{\max}(\cdot)$, and three reference points are labeled in red.

censored likelihood, agrees with this observation; nonstationary model 3 generally outperforms all other models using the GSM inference method, followed by nonstationary model 1 with approximately the same performance, while nonstationary models using the WLS inference method generally require the warping function with more complex architectures to perform better. In general, estimated warped spaces obtained using the GSM inference method better match the true warped space and are less prone to overfitting; we observe generally lower censored likelihoods when modeling with the more complex Architectures 2 and 4, compared to the oracle Architecture 3.

Estimates of the extremal dependence parameters, φ and κ , are also summarized in Table 3 for each risk functional and both inference methods. We observe generally less bias in estimates of the smoothness κ , and smaller standard deviations of dependence

Table 2: Test censored log-likelihoods (larger is preferred) evaluated for all fitted models, using both the gradient score matching (GSM) and weighted least squares (WLS) inference methods, and with three different risk functionals. The best models are highlighted in bold for each risk functional and each inference method, and the oracle model based on Architecture 3 is labeled with an asterisk.

Architecture	Inference method	Risk functional		
		$r_{\text{site}}(\cdot)$	$r_{\text{max}}(\cdot)$	$r_{\text{sum}}(\cdot)$
Stationary	WLS	-49229	-14305	15043
Nonstationary 1		- 46595	-13645	17462
Nonstationary 2		-46603	-13670	17401
Nonstationary 3*		-47829	-13719	17440
Nonstationary 4		-47150	- 13616	17379
Stationary	GSM	-48519	-14081	15046
Nonstationary 1		-44943	-12677	18088
Nonstationary 2		-45050	-12736	17962
Nonstationary 3*		- 44914	- 12673	18107
Nonstationary 4		-45063	-12718	18000

Table 3: Estimates of the extremal dependence parameters, $\hat{\psi} = (\hat{\varphi}, \hat{\kappa})$, for data generated with Architecture 1, using both the gradient score matching (GSM) and weighted least squares (WLS) inference methods, and three different risk functionals. The true values of the extremal dependence parameters are $\varphi_0 = 0.2$ and $\kappa_0 = 1$. Standard deviations obtained using a nonparametric bootstrap are reported in brackets as subscripts of the corresponding parameter estimate.

Architecture	Inference method	Risk functional		
		$r_{\text{site}}(\cdot)$	$r_{\text{max}}(\cdot)$	$r_{\text{sum}}(\cdot)$
Stationary	WLS	0.282 _(0.039) , 1.155 _(0.104)	0.293 _(0.053) , 1.166 _(0.093)	0.274 _(0.056) , 1.029 _(0.075)
Nonstationary 1		0.176 _(0.042) , 1.129 _(0.120)	0.266 _(0.049) , 1.228 _(0.118)	0.195 _(0.052) , 0.990 _(0.086)
Nonstationary 2		0.170 _(0.044) , 1.099 _(0.124)	0.259 _(0.044) , 1.215 _(0.119)	0.196 _(0.049) , 0.985 _(0.092)
Nonstationary 3		0.204 _(0.030) , 1.168 _(0.128)	0.257 _(0.048) , 1.225 _(0.125)	0.206 _(0.052) , 0.994 _(0.091)
Nonstationary 4		0.189 _(0.028) , 1.128 _(0.127)	0.256 _(0.045) , 1.213 _(0.127)	0.204 _(0.049) , 0.992 _(0.092)
Stationary	GSM	0.203 _(0.002) , 1.053 _(0.004)	0.204 _(0.002) , 1.056 _(0.005)	0.203 _(0.002) , 1.054 _(0.004)
Nonstationary 1		0.204 _(0.003) , 1.053 _(0.006)	0.205 _(0.003) , 1.056 _(0.007)	0.206 _(0.003) , 1.055 _(0.006)
Nonstationary 2		0.201 _(0.004) , 1.047 _(0.009)	0.203 _(0.003) , 1.058 _(0.009)	0.204 _(0.003) , 1.053 _(0.008)
Nonstationary 3		0.206 _(0.002) , 1.045 _(0.004)	0.205 _(0.001) , 1.046 _(0.004)	0.205 _(0.002) , 1.045 _(0.004)
Nonstationary 4		0.205 _(0.003) , 1.051 _(0.006)	0.203 _(0.002) , 1.050 _(0.006)	0.204 _(0.002) , 1.049 _(0.006)

parameter estimates when using the GSM inference method. This supports the use of the GSM inference method due to its robust performance in terms of both warped space and parameter estimation, albeit at a computational cost approximately 20% higher.

Figure 2 provides a detailed look at the estimated extremal dependence structure, rel-

ative to three reference sites; for each reference site, we evaluate the pairwise CEPs with respect to all other sites, where the data are generated with risk the functional $r_{\max}(\cdot)$ and are fitted using nonstationary model 1 (with Architecture 1), and inference method GSM. Estimated pairwise CEPs generally match the oracle pattern very well. Furthermore, extreme events at reference sites exhibit strong yet nonstationary extremal dependence with nearby locations. For instance, extremes observed at reference sites 1 and 2 show pronounced spatial dependence, with the “valley” and “edge” regions varying dynamically across the direction and distance. Uncertainty in the warped space is assessed via the standard deviation of fitted pairwise CEP estimates using a nonparametric bootstrap (with the fixed warping). These results reveal markedly lower variability in CEP estimates for pairs of sites exhibiting similar extremal behavior (indicative of strong dependence). In contrast, higher uncertainty emerges for pairs where one site lies within gradient regions of the warped space, i.e., areas characterized by abrupt transitions in extremal dependence structure.

Compared to Architecture 3, Architecture 1 includes an additional MT unit, with its warped-domain estimates shown in Figure S1. We see pronounced differences in the estimated warped spaces between architectures with and without an MT unit (e.g., models 1 vs. 3, or 2 vs. 4). Table S1 quantifies and agrees with this: nonstationary models incorporating an MT unit consistently achieve superior fit. Conversely, when fitting data generated without an MT unit, models that include an MT unit perform on par with those using the true (no MT unit) architecture. These results therefore recommend the inclusion of an MT unit in practice.

When the true extremal dependence structure is highly complex, as seen when data are generated under Architectures 2 and 4, visual estimates of the complex warped space favor the WLS inference method, as it better recovers the intricate dependence patterns (see Figures S2 and S3 in the Supplementary Material). However, biased estimation of extremal dependence parameters, particularly the smoothness parameter κ , using WLS (see Tables S4, S6) yields lower censored likelihood values compared to those obtained using GSM (see Tables S3, S5). In these scenarios, oversimplified architectures do not

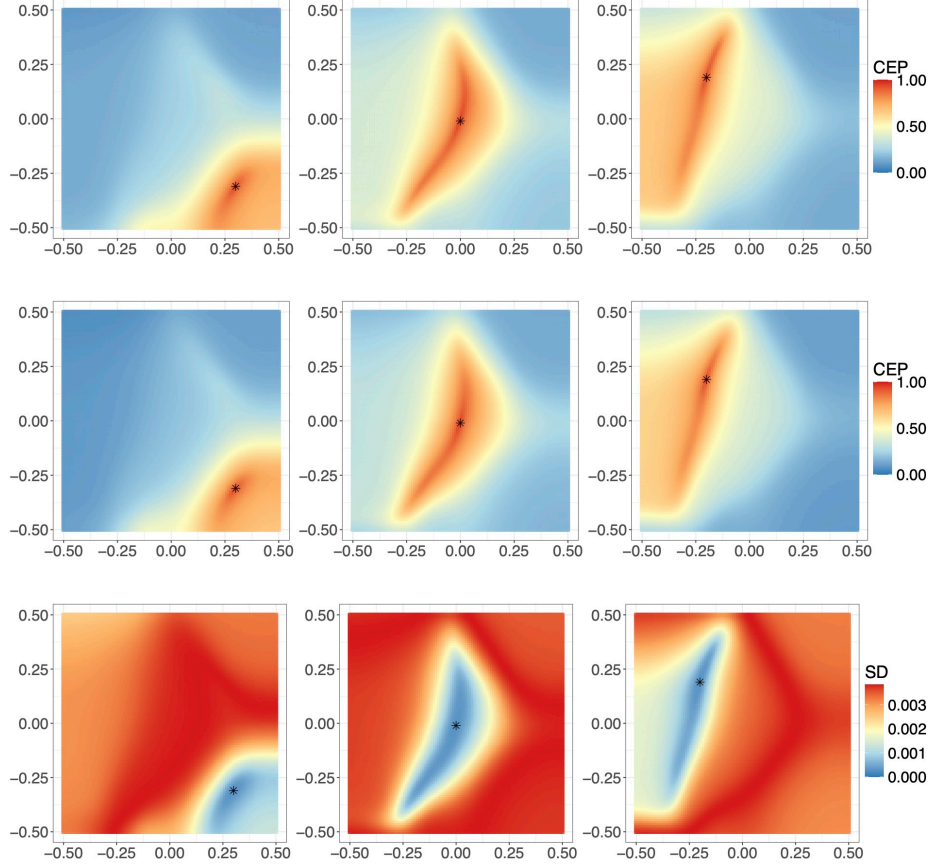


Figure 2: Theoretical (top row) and estimated (middle row) pairwise CEPs in (3) relative to site 1 (left column), site 2 (central column), and site 3 (right column) denoted by the asterisk. Third row: standard deviation (SD) of estimated pairwise CEPs. The data are generated with Architecture 3 with the risk functional $r_{\max}(\cdot)$, and the model is fitted using nonstationary model 1 and the GSM method.

suffice to estimate the complicated warped space, while architectures with the SR-RBF(2) unit generally perform better.

5 Data application

5.1 UK precipitation extremes

We demonstrate the efficacy of our proposed model via an analysis of precipitation data from the 2018 UK climate projections (UKCP18; [Lowe et al., 2019](#)), which contains values

produced at hourly intervals on $2.2 \times 2.2 \text{ km}^2$ grid boxes between the years 1980 and 2000; these data were also studied by [Richards and Wadsworth \(2021\)](#), in the context of nonstationary extremal dependence modeling, and [Richards and Tawn \(2022\)](#) and [Richards et al. \(2023\)](#), for inferring extremes of the risk functional $r_{\text{sum}}(\cdot)$. The data can be downloaded freely from the CEDA data catalogue; see [Met Office Hadley Centre \(2019\)](#). We focus on extreme rainfall over the west of Great Britain. As distance from the sea, proximity of mountains, and elevation are known drivers of extreme rainfall ([Faulkner and Prudhomme, 1998](#)), we choose our study domain so that it includes complex topography which should induce nonstationarity in the spatial rainfall distribution: the coast of Wales and the Cambrian Mountains, and the West Midlands region to the west of the mountains; see Figure 3. We further visualize the cumulative rainfall over the year 2000 in Figure 3, which shows that the aforementioned factors influence the intensity of the precipitation distribution. The air carrying large amounts of water vapor from the Atlantic Ocean from west to east is lifted by the Cambrian Mountains, forming denser rainfall on the west side of the mountains. Therefore, rainfall anomalies are also concentrated in this area.

To reduce the number of zeros in the data, observations are aggregated to daily accumulated rainfall. Moreover, we take only the summer months, from June to August, to avoid seasonal effects; this leads to $N = 1800$ temporal replicates. We randomly sample $D_{\text{train}} = 2000$ sites, from the total of $D = 12600$ available sites, as the training set, and $D_{\text{test}} = 100$ sites for testing. Data margins are standardized to be standard Pareto using i) the empirical distribution function below a marginal threshold (95% empirical quantile) and ii) a fitted generalized Pareto distribution (GPD) to excesses above the threshold (see, e.g., [Coles, 2001](#)). Specifically, the marginal model for rainfall exceedances $Y(\mathbf{s}_i)$ over a high threshold $u(\mathbf{s}_i)$ at site $\mathbf{s}_i \in \mathcal{S}$ is $\{Y(\mathbf{s}_i) - u(\mathbf{s}_i)\} \mid Y(\mathbf{s}_i) > u(\mathbf{s}_i) \stackrel{\text{ind}}{\sim} \text{GPD}\{\tau(\mathbf{s}_i), \xi(\mathbf{s}_i)\}$ for all $i = 1, \dots, D$, which has the distribution function

$$G\{y; \tau(\mathbf{s}_i), \xi(\mathbf{s}_i)\} = \begin{cases} 1 - \{1 + \xi(\mathbf{s}_i)y/\tau(\mathbf{s}_i)\}_+^{-1/\xi(\mathbf{s}_i)}, & \xi(\mathbf{s}_i) \neq 0, \\ 1 - \exp\{-y/\tau(\mathbf{s}_i)\}, & \xi(\mathbf{s}_i) = 0, \end{cases} \quad (11)$$

where the scale parameter $\tau(\mathbf{s}_i) > 0$ and shape parameter $\xi(\mathbf{s}_i) \in \mathbb{R}$ are spatially-varying,

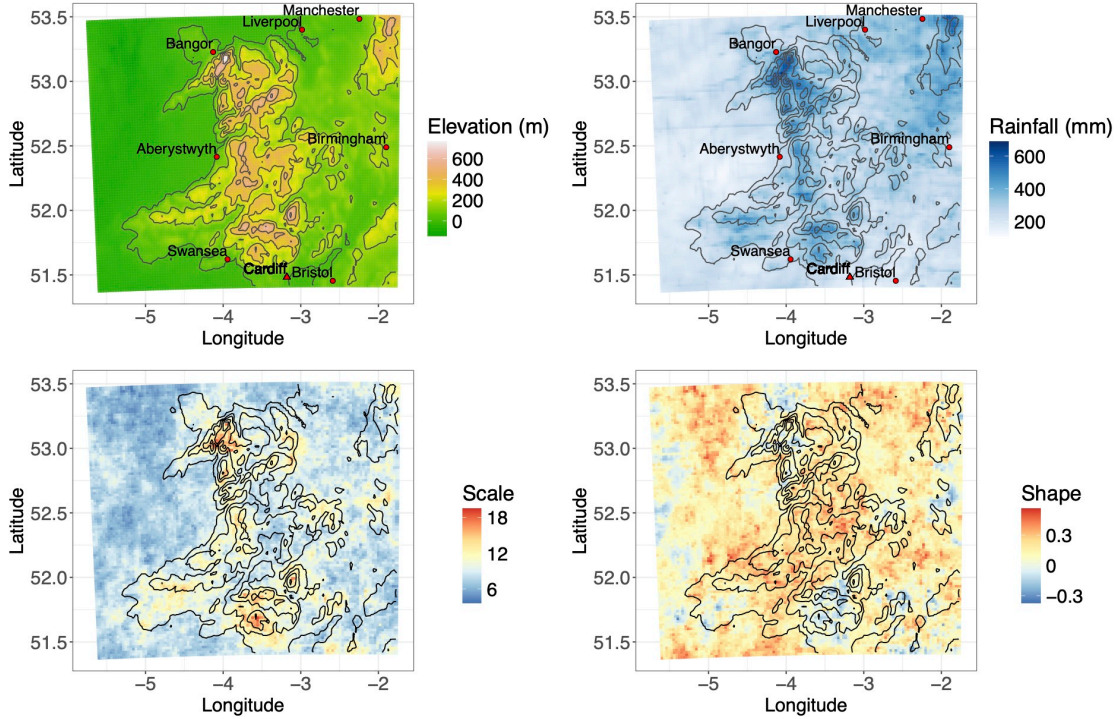


Figure 3: Top row: topography of the study domain (left panel), and the cumulative rainfall for 2020 (mm; right panel). Bottom row: estimated scale parameter $\tau(s_i)$ and shape parameter $\xi(s_i)$ of (marginal) generalized Pareto distribution for $i \in 1, \dots, D$. Elevation contour lines are plotted (in black) in each panel for reference.

and $\{\cdot\}_+ = \max\{\cdot, 0\}$. Parameter estimates are presented in Figure 3. Larger scale and shape estimates to the west of the Cambrian Mountains suggest more extreme rainfall there, aligning with our explanatory analysis. Only five of 12600 locations violate the null hypothesis that the data at these sites do not follow a GPD. In the Supplementary Material, Figure S4 shows model diagnostic plots for these sites, and Figure S5 presents quantile-quantile (Q-Q) plots of the data for the total domain and at six representative sites. We then model the transformed data $X(s_i) = 1/[1 - F_{s_i}\{Y(s_i)\}]$, for $i = 1, \dots, D$, using deep compositional Brown–Resnick r -Pareto processes, as described in Section 2.

5.2 Extremal dependence modeling

For defining extreme events, we consider the three risk functionals $r_{\text{site}}(\cdot)$, $r_{\text{max}}(\cdot)$, and $r_{\text{sum}}(\cdot)$ in (12). For $r_{\text{site}}(\cdot)$, we choose the reference site s_0 to be Cardiff, the capital city

Table 4: Model fit metrics including censored log-likelihoods (CL; larger is preferred), square errors (SE; smaller is preferred), and gradient scores (GS; smaller is preferred) estimated on test data for fitted models with various architectures for $\mathbf{f}(\cdot)$, using both the gradient score matching (GSM) and weighted least squares (WLS) inference methods, and three different risk functionals. The best models are highlighted in bold for each risk functional and inference method.

Architecture	Inference method	Risk functional								
		$r_{\text{site}}(\cdot)$			$r_{\text{max}}(\cdot)$			$r_{\text{sum}}(\cdot)$		
		CL	SE	GS	CL	SE	GS	CL	SE	GS
Stationary	WLS	-38094	90.37	-0.07	-7210	81.18	-0.30	-25908	74.92	-0.32
Nonstationary 1		-38097	93.06	-0.09	-7211	68.77	-0.45	-26007	65.60	-0.47
Nonstationary 2		-38156	90.36	-0.07	-7205	66.85	-0.49	-25986	60.11	-0.46
Nonstationary 3		-38151	94.24	-0.14	-7228	75.58	-0.39	-26019	69.09	-0.46
Nonstationary 4		-38301	90.57	-0.15	-7214	71.13	-0.49	-26054	61.74	-0.55
Stationary	GSM	-38441	94.73	-1.00	-7445	103.95	-1.00	-26804	95.42	-1.00
Nonstationary 1		-38567	96.50	-1.06	-7396	93.70	-0.94	-26824	93.78	-1.23
Nonstationary 2		-38594	93.85	-1.11	-7403	98.03	-1.10	-26823	92.91	-1.22
Nonstationary 3		-38601	95.89	-1.07	-7452	100.26	-1.09	-26897	96.33	-1.27
Nonstationary 4		-38586	97.00	-1.04	-7403	94.14	-1.06	-26832	94.42	-1.24

of Wales (see Figure 3). We also consider the max-functional $r_{\text{max}}(\cdot)$ computed at all D remaining sites, \mathcal{D}_0 , and the modified sum-functional $r_{\text{sum};\beta}(\cdot)$ with $\beta = D^{-1} \sum_{i=1}^D \hat{\xi}(\mathbf{s}_i) = 0.174$ taken to be the average of independent local estimates of the shape parameter from the fitted GPD marginal model. We therefore consider the following risk functionals:

$$r_{\text{site}}(X) = X(\mathbf{s}_0), \quad r_{\text{max}}(X) = \max_{\mathbf{s} \in \mathcal{D}_0} X(\mathbf{s}), \quad \text{and} \quad r_{\text{sum};\beta}(X) = \left\{ \sum_{\mathbf{s} \in \mathcal{D}_0} X(\mathbf{s})^\beta \right\}^{1/\beta}. \quad (12)$$

The threshold u is taken in each case to be the 90% quantile of observed r -exceedances, leaving $N_u = 180$ functional exceedances for model fitting, and u' is set to the empirical 95% marginal quantile. We conduct inference with i) the WLS method, where we pre-estimate the empirical CEPs using the training set, and ii) the GSM method. Similar to the simulation study, we consider the four different compositional architectures for the warping \mathbf{f} as shown in Table 1. As a comparison, stationary models are also fitted to the data.

Table 4 provides model fit metrics over the test data for all fitted stationary and non-stationary models, in terms of censored likelihoods, and additionally, (weighted) gradient scores defined in Equation (8) and square errors of empirical and fitted CEPs, using both in-

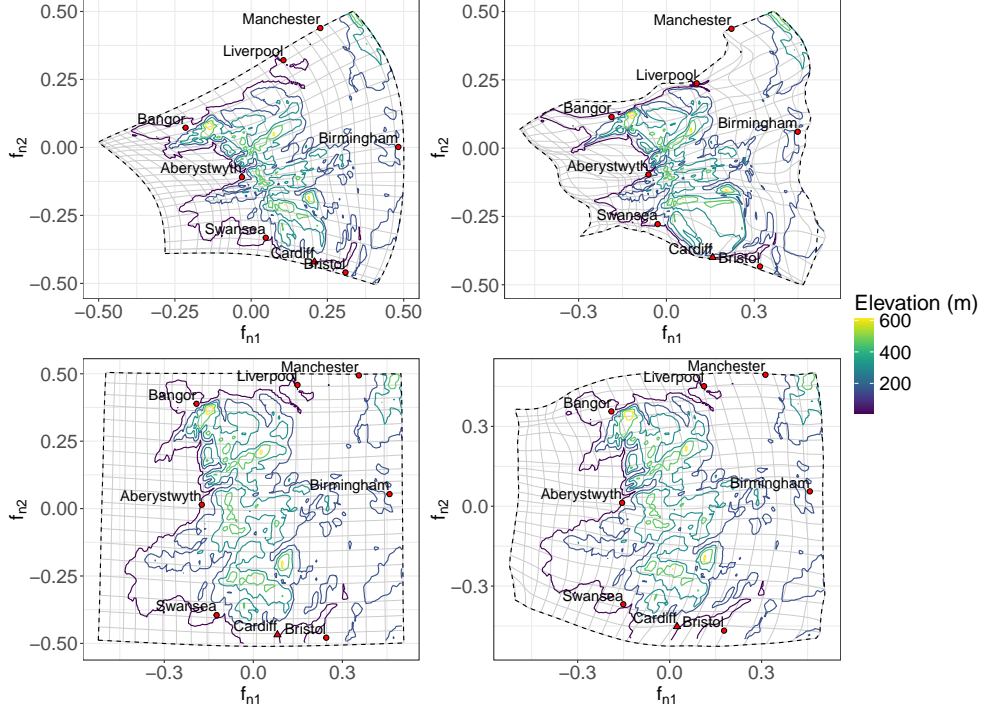


Figure 4: Estimated warped space with nonstationary model 1 (left column) and 2 (right column), the WLS (top row) and GSM (bottom row) inference methods, and using the $r_{\max}(\cdot)$ risk functional. Warped longitude and latitude lines are given, elevation contour lines are colored according to their magnitude, and some reference cities are labeled in red.

ference methods, and all risk functionals. While the improvement of nonstationary models does not seem to be substantial compared to stationary models, these metrics still suggest that nonstationary models perform better at unobserved locations, especially for the max-functional. This out-of-sample improvement is especially interesting given that these nonstationary models are much more complex and have a much larger number of parameters than their stationary counterparts. While the censored likelihood metric suggests that the stationary models are better when using the site- and sum-functionals, it only assesses the models' performance in cases where all sites experience extreme events simultaneously. When partial extremes occur, the gradient score metric suggests that nonstationary models are better. The square error metric also supports this conclusion. Among nonstationary models, we can also see that models 1 and 2 (those that include the MT unit) outperform the other two in general.

Table 5: Estimates of the extremal dependence parameters, $\hat{\psi} = (\hat{\varphi}, \hat{\kappa})$, using both the gradient score matching (GSM) and weighted least squares (WLS) inference methods, and three different risk functionals. Standard deviations obtained using a nonparametric bootstrap are reported in brackets as subscripts of the corresponding parameter estimate.

Architecture	Inference method	Risk functional		
		$r_{\text{site}}(\cdot)$	$r_{\text{max}}(\cdot)$	$r_{\text{sum}}(\cdot)$
Stationary	WLS	0.100 _(0.018) , 0.688 _(0.127)	0.108 _(0.025) , 0.730 _(0.102)	0.110 _(0.021) , 0.756 _(0.110)
Nonstationary 1		0.084 _(0.010) , 0.679 _(0.112)	0.088 _(0.010) , 0.746 _(0.089)	0.096 _(0.008) , 0.762 _(0.098)
Nonstationary 2		0.074 _(0.010) , 0.644 _(0.109)	0.081 _(0.010) , 0.718 _(0.083)	0.091 _(0.007) , 0.741 _(0.089)
Nonstationary 3		0.110 _(0.008) , 0.686 _(0.127)	0.113 _(0.010) , 0.758 _(0.104)	0.113 _(0.009) , 0.790 _(0.112)
Nonstationary 4		0.091 _(0.007) , 0.662 _(0.117)	0.098 _(0.009) , 0.728 _(0.096)	0.100 _(0.008) , 0.758 _(0.099)
Stationary	GSM	0.175 _(0.002) , 0.991 _(0.024)	0.159 _(0.002) , 0.939 _(0.013)	0.178 _(0.002) , 1.009 _(0.034)
Nonstationary 1		0.171 _(0.005) , 0.985 _(0.031)	0.152 _(0.002) , 0.912 _(0.008)	0.176 _(0.003) , 1.010 _(0.037)
Nonstationary 2		0.168 _(0.003) , 0.973 _(0.030)	0.151 _(0.002) , 0.914 _(0.011)	0.173 _(0.004) , 1.008 _(0.043)
Nonstationary 3		0.177 _(0.004) , 0.997 _(0.024)	0.162 _(0.002) , 0.943 _(0.009)	0.181 _(0.003) , 1.014 _(0.033)
Nonstationary 4		0.171 _(0.003) , 0.988 _(0.024)	0.152 _(0.002) , 0.913 _(0.011)	0.176 _(0.004) , 1.011 _(0.037)

Figure 4 demonstrates the estimated warped spaces using nonstationary models 1 and 2, using both the WLS and GSM inference methods, with the $r_{\text{max}}(\cdot)$ risk functional. The warped spaces estimated using two inference methods are relatively different: the WLS inference method tends to provide more prominent deformation than GSM, aligning with results for simulated data using more complex architectures (recall Section 4). All warped spaces estimated with extremes defined via $r_{\text{max}}(\cdot)$ show a prominent contraction of the ocean and coastal area to the west of the mountains while a prominent expansion of the east plain area (by observing warped longitude and latitude lines), indicating that there is relatively stronger extremal dependence to the west of the mountains. Furthermore, the mountainous region is horizontally expanded, suggesting that rainfall extremes on both sides are blocked by the mountainous landform and are hence less dependent.

Dependence parameters estimates, $\hat{\psi} = (\hat{\varphi}, \hat{\kappa})$, are also reported in Table 5, together with their standard deviation evaluated using a nonparametric bootstrap, in which the warpings are re-estimated to account for the uncertainty brought by the deformation. Generally speaking, the effect of the deformation on the uncertainty of the dependence parameter estimates, with various complex structures, does not appear significant; deviations of the parameters using either stationary or nonstationary models do not show obvious differences in magnitude. Note that the range parameter may alter with the scale

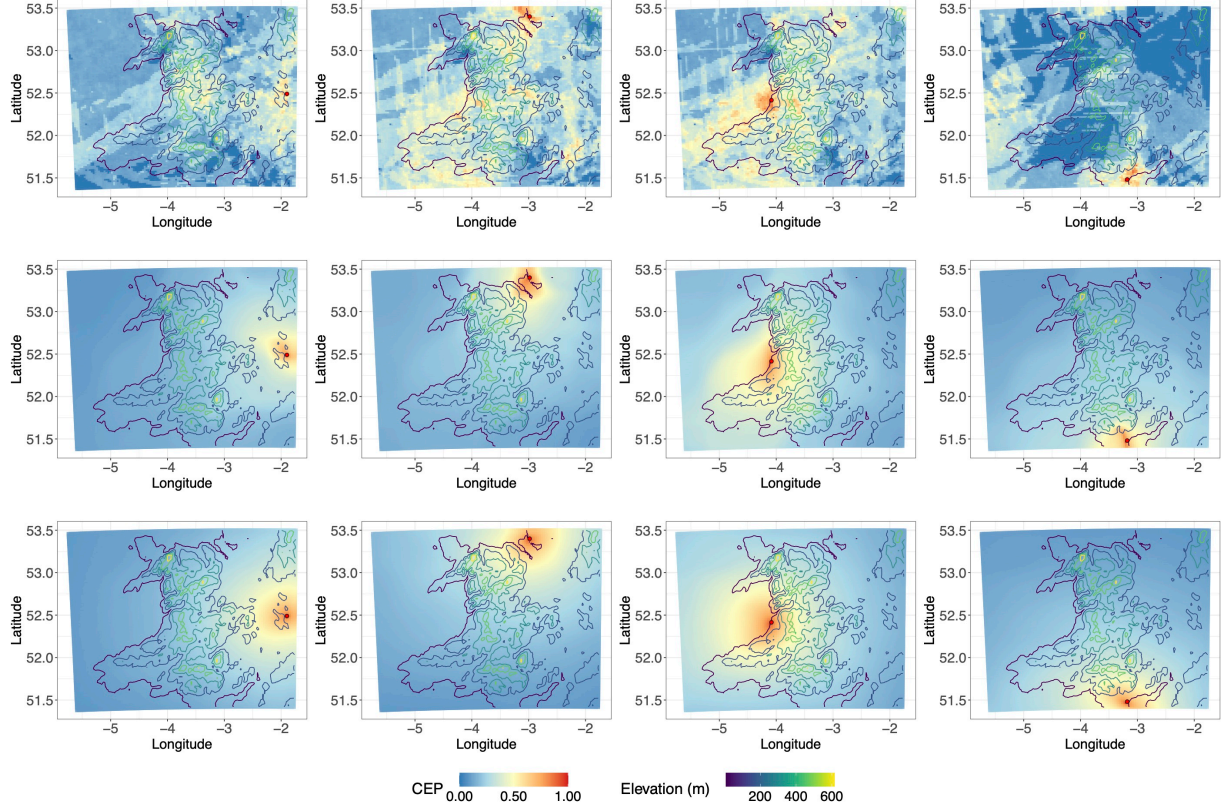


Figure 5: Empirical (first row) and fitted pairwise CEPs relative to Birmingham (1st column), Liverpool (2nd column), Aberystwyth (3th column), and Cardiff (4th column), using the nonstationary model 4 and inference method WLS and GSM, where the extremes are defined through $r_{\max}(\cdot)$. Elevation contour lines are colored with their magnitude information as references.

of the warped space, and rescaling of the warped space may be considered to stabilize the estimation of range parameters. Yet, the extremal dependence structure only depends on the relative positions among warped locations, and the range estimates are also adapted to different space scales, which would not affect the evaluated extremal dependence structure. Similar to the results of the simulation study, the deviation of the dependence parameter estimates for models fitted using the GSM inference method is generally smaller than those fitted using the WLS inference method.

In Figure 5, we further present the detailed extremal dependence structure estimated using nonstationary model 2 and risk functional $r_{\max}(\cdot)$, with respect to the following refer-

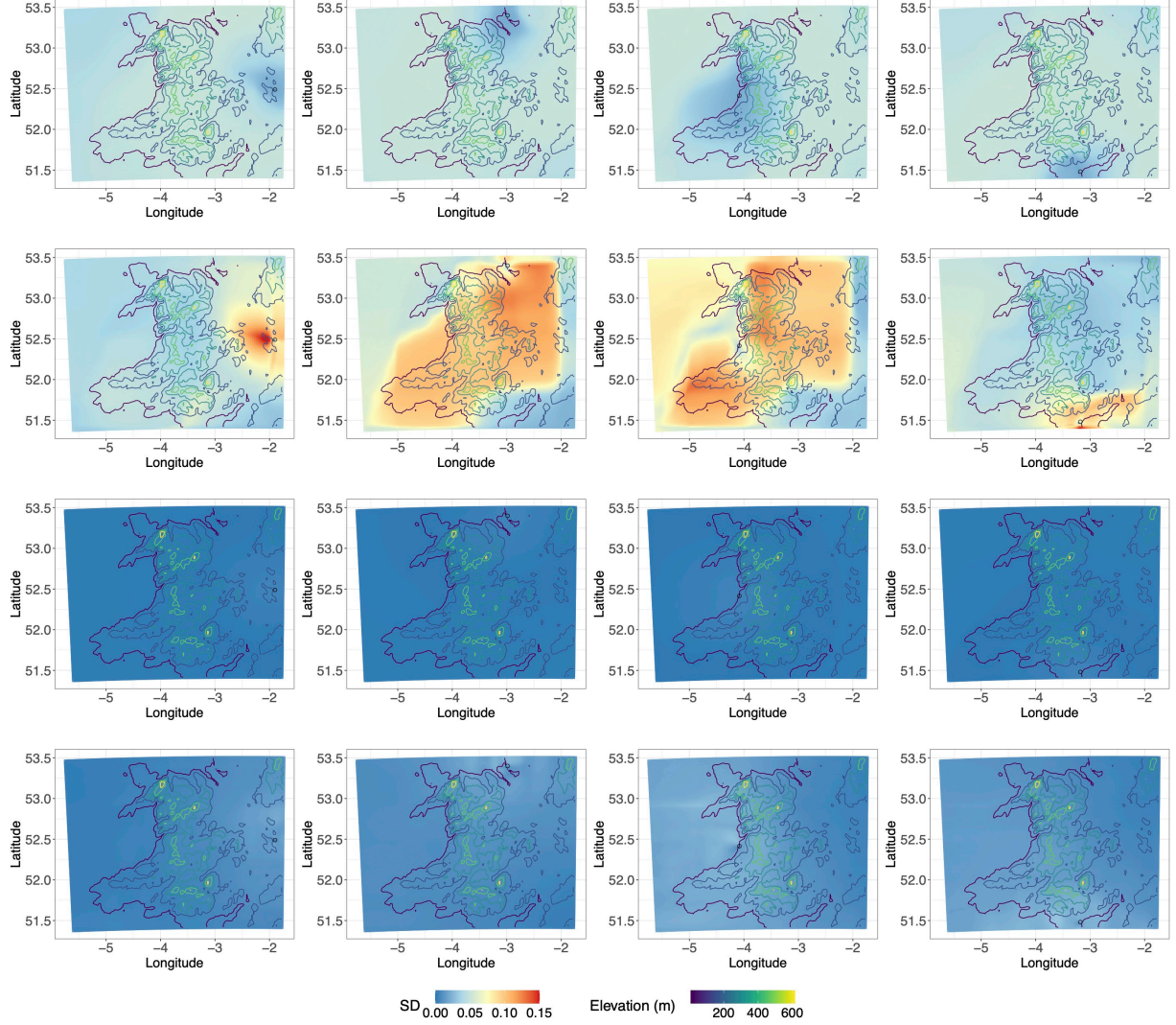


Figure 6: Standard deviation of the fitted pairwise CEPs without (1st and 3rd rows) and with (2nd and 4th rows) the consideration of the deformation for reference cities Birmingham (1st column), Liverpool (2nd column), Aberystwyth (3th column), and Cardiff (4th column) using either WLS (1st and 2nd rows) or GSM (3rd and 4th rows) inference method. Elevation contour lines are colored with their magnitude information as references.

ence cities: Birmingham, Liverpool, Aberystwyth, and Cardiff. The results are represented by maps of pairwise CEPs relative to the aforementioned reference cities, which show that the fitted nonstationary models capture the anisotropy and nonstationarity in the extremal dependence structure quite well. We can further observe the prominent effect of landform on extremal dependence; due to the mountain barrier, the rainfall anomaly in Aberystwyth

is highly correlated in a large area to the west, while the rainfall anomaly in Birmingham is only highly correlated with a small adjacent terrestrial area in the east. Uncertainty assessment is reported, in terms of standard deviations computed using a nonparametric bootstrap, as discussed in Section 3.3, and these are shown for pairwise CEPs in Figure 6. We observe smaller standard deviations near the reference city, and larger uncertainty further away. The uncertainty pattern aligns with that of the estimated extremal dependence structure, which is influenced by the warped space. In contrast to the minimal impact observed on uncertainty for estimated dependence parameters, Figure 6 indicates that the deformation plays a substantially larger role in inflating the uncertainty of pairwise CEPs: when taking the impact of the deformation into account, the standard deviations in estimated CEPs are markedly greater than those obtained that the assuming warping fixed. Furthermore, the standard deviation is usually smaller when using the GSM inference method compared to the WLS method, which aligns with our previous conclusion that the performance of the GSM method is more robust than the WLS method. To visualize the performance of our fitted models over the warped space, Figure 7 presents the empirical CEP estimates, $\hat{\pi}_{ij}(u, u')$, against distance computed both in the (rescaled) original and warped spaces, estimated using nonstationary model 2 and $r_{\max}(\cdot)$ (for which the nonstationary models outperform the stationary ones). Estimates are grouped by distance and presented using box plots. The more concentrated the points around the reference line of the relative estimated CEP function, i.e., the reference line passing through the main box and error bars shrinking by distance, the more stationary the behavior of spatial extremes over that space. We see that the empirical CEPs-distance plots over the estimated warped space using both inference methods appear to be more concentrated around the reference line, especially for the distant pairs. We further quantify the concentration by reporting the mean absolute difference between the empirical estimates and the theoretical one that comes from the reference curves: results show that the mean absolute difference for nonstationary models are approximately 0.085 and 0.100 when using the WLS and GSM methods, respectively, outperforming 0.097 and 0.103 for the stationary model using the WLS or GSM methods. We hence conclude that the deformation has created processes

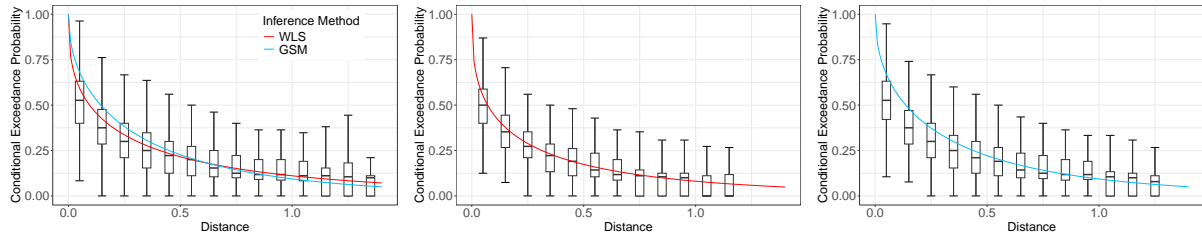


Figure 7: Estimates of pairwise conditional exceedance probabilities $\hat{\pi}_{ij}(u, u')$ against relative distances in both (rescaled) original space (left panel) and estimated warped spaces using nonstationary model 2, with WLS (centre panel) and GSM (right panel) inference methods, respectively. The reference lines of theoretical pairwise CEPs against the distance are added based on corresponding estimated dependence parameters.

that appear to be more stationary with regard to their respective CEP estimates in the new warped domain.

6 Concluding remarks

In this work, we proposed a deformation approach to model nonstationarity in the extremal spatial dependence of high dimensional data based on the deep compositional spatial model (DCSM). We developed a flexible and computationally efficient method to estimate the nonstationary extremal dependence by warping the original spatial domain to a latent space where stationarity and isotropy in the extremal dependence structure can be reasonably assumed. By leveraging the DCSM framework, we efficiently estimated the warping function while ensuring injectivity and hence overcame the space-folding issue prevailing in previous research. We proposed practical strategies to assess the uncertainty of the estimated extremal dependence structure using bootstrapping. We leveraged Brown–Resnick r -Pareto processes for extremal dependence modeling, in order to characterize spatial peak-over-threshold events, and we performed inference by loss minimization, using either a weighted least squares error loss or a gradient score matching loss. The proposed framework is also compatible with other spatial extremal processes, e.g., max-stable or asymptotically independent processes (e.g., scale mixtures), subject to simple modifications of the loss function. In both our simulation study and real data application, we showed that our pro-

posed methodology succeeds in providing good fits and capturing complex nonstationary extremal dependence structures.

Future work includes an extension to incorporate temporal nonstationarity and jointly characterize nonstationary spatio-temporal extremal dependence patterns. In the Gaussian setting, [Vu et al. \(2023\)](#) constructed nonstationary spatio-temporal covariance models via compositional warpings, which only allows rescaling time using axial warping units, yet non-separable space-time modeling is usually required for applications. Furthermore, it would be interesting to extend our methodology to incorporate covariates, e.g., elevation, into the estimated warping for enhanced interpretability. Last but not least, current modeling approaches in spatial statistics using deep learning techniques require training the network over a specific study domain, but it cannot easily be extended to other regions. Retraining an alternative model is time-consuming for new datasets. Transfer-learning approaches that can properly exploit pretrained models for inference in a new spatial domain would be of interest.

To promote reproducibility, our code and data are made fully available at the following GitHub repository: <https://github.com/shaox0a/DCSMEExt/>.

Acknowledgement

The authors are grateful to Simon Brown for help in accessing the UK precipitation data, and to Andrew Zammit-Mangion and Quan Vu for helpful discussions on the methodology.

References

- Bornn, L., G. Shaddick, and J. V. Zidek (2012). Modeling nonstationary processes through dimension expansion. *Journal of the American Statistical Association* 107(497), 281–289.
- Brown, B. M. and S. I. Resnick (1977). Extreme values of independent stochastic processes. *Journal of Applied Probability* 14(4), 732–739.
- Buhl, S. and C. Klüppelberg (2016). Anisotropic Brown-Resnick space-time processes: estimation and model assessment. *Extremes* 19, 627–660.
- Chevalier, C., O. Martius, and D. Ginsbourger (2021). Modeling nonstationary extreme dependence with stationary max-stable processes and multidimensional scaling. *Journal of Computational and Graphical Statistics* 30(3), 745–755.

- Coles, S. (2001). *An Introduction to Statistical Modeling of Extreme Values*, Volume 208. Springer.
- de Fondeville, R. and A. C. Davison (2018). High-dimensional peaks-over-threshold inference. *Biometrika* 105(3), 575–592.
- de Fondeville, R. and A. C. Davison (2022). Functional peaks-over-threshold analysis. *Journal of the Royal Statistical Society Series B: Methodology* 84(4), 1392–1422.
- Dombry, C., J. Legrand, and T. Opitz (2024). Pareto processes for threshold exceedances in spatial extremes. *arXiv preprint arXiv:2407.05699*.
- Dombry, C. and M. Ribatet (2015). Functional regular variations, Pareto processes and peaks over threshold. *Statistics and its Interface* 8(1), 9–17.
- Engelke, S., A. Malinowski, Z. Kabluchko, and M. Schlather (2015). Estimation of Hüsler–Reiss distributions and Brown–Resnick processes. *Journal of the Royal Statistical Society Series B: Methodology* 77(1), 239–265.
- Faulkner, D. and C. Prudhomme (1998). Mapping an index of extreme rainfall across the UK. *Hydrology and Earth System Sciences* 2(2/3), 183–194.
- Ferreira, A. and L. de Haan (2014). The generalized Pareto process; with a view towards application and simulation. *Bernoulli* 20(4), 1717–1737.
- Forster, C. and M. Oesting (2025). Non-stationary max-stable models with an application to heavy rainfall data. *Extremes*, To appear.
- Huser, R. and M. G. Genton (2016). Non-stationary dependence structures for spatial extremes. *Journal of Agricultural, Biological, and Environmental Statistics* 21, 470–491.
- Huser, R., T. Opitz, and J. L. Wadsworth (2025). Modeling of spatial extremes in environmental data science: time to move away from max-stable processes. *Environmental Data Science* 4, e3.
- Hyvärinen, A. (2007). Some extensions of score matching. *Computational statistics & data analysis* 51(5), 2499–2512.
- Hyvärinen, A. and P. Dayan (2005). Estimation of non-normalized statistical models by score matching. *Journal of Machine Learning Research* 6(4), 695–709.
- Iovleff, S. and O. Perrin (2004). Estimating a nonstationary spatial structure using simulated annealing. *Journal of Computational and Graphical Statistics* 13(1), 90–105.
- Kingma, D. P. and J. Ba (2015). Adam: A method for stochastic optimization. *arXiv preprint arXiv:1412.6980*.
- Lowe, J., D. Bernie, P. E. Bett, L. M. Bricheno, S. Brown, D. Calvert, R. D. Clark, Karen, Eagle, T. Edwards, G. Fossler, P. Maisey, R. McInnes, C. F. McSweeney, K. Yamazaki, and S. Belcher (2019). UKCP18 science overview report.
- Met Office Hadley Centre (2019). UKCP Convection-Permitting Model Projections for the UK at 2.2km resolution. NERC EDS Centre for Environmental Data Analysis. <https://catalogue.ceda.ac.uk/uuid/ad2ac0ddd3f34210b0d6e19bfc335539>. Last accessed 16/05/2025.

- Opitz, T. (2013). Extremal t processes: Elliptical domain of attraction and a spectral representation. *Journal of Multivariate Analysis* 122, 409–413.
- Paciorek, C. J. and M. J. Schervish (2006). Spatial modelling using a new class of nonstationary covariance functions. *Environmetrics* 17(5), 483–506.
- Parker, R. J., B. J. Reich, and J. Eidsvik (2016). A fused LASSO approach to nonstationary spatial covariance estimation. *Journal of Agricultural, Biological, and Environmental Statistics* 21(3), 569–587.
- Perrin, O. and P. Monestiez (1999). Modelling of non-stationary spatial structure using parametric radial basis deformations. In J. Gómez-Hernández, A. Soares, and R. Froidevaux (Eds.), *GeoENV II: Geostatistics for Environmental Applications*, pp. 175–186. New York: Springer.
- Richards, J. and J. A. Tawn (2022). On the tail behaviour of aggregated random variables. *Journal of Multivariate Analysis* 192, 105065.
- Richards, J., J. A. Tawn, and S. Brown (2023). Joint estimation of extreme spatially aggregated precipitation at different scales through mixture modelling. *Spatial Statistics* 53, 100725.
- Richards, J. and J. L. Wadsworth (2021). Spatial deformation for nonstationary extremal dependence. *Environmetrics* 32(5), e2671.
- Sampson, P. D. and P. Guttorp (1992). Nonparametric estimation of nonstationary spatial covariance structure. *Journal of the American Statistical Association* 87(417), 108–119.
- Saunders, K., A. Stephenson, and D. Karoly (2021). A regionalisation approach for rainfall based on extremal dependence. *Extremes* 24, 215–240.
- Schlather, M. (2002). Models for stationary max-stable random fields. *Extremes* 5(1), 33–44.
- Schmidt, A. M. and A. O’Hagan (2003). Bayesian inference for non-stationary spatial covariance structure via spatial deformations. *Journal of the Royal Statistical Society: Series B: Methodology* 65(3), 743–758.
- Sefton, C., K. Muchan, S. Parry, B. Matthews, L. Barker, S. Turner, and J. Hannaford (2021). The 2019/2020 floods in the UK: a hydrological appraisal. *Weather* 76(12), 378–384.
- Shao, X., A. Hazra, J. Richards, and R. Huser (2025). Flexible modeling of nonstationary extremal dependence using spatially fused LASSO and ridge penalties. *Technometrics* 67(1), 97–111.
- Smith, R. L. (1990). Max-stable processes and spatial extremes. *Unpublished manuscript*. <https://www.rls.sites.oasis.unc.edu/postscript/rs/spatex.pdf>.
- Smith, R. L. (1996). Estimating nonstationary spatial correlations. *Preprint, University of North Carolina* 76.
- Vu, Q., A. Zammit-Mangion, and S. J. Chuter (2023). Constructing large nonstationary spatio-temporal covariance models via compositional warpings. *Spatial Statistics* 54, 100742.

- Vu, Q., A. Zammit-Mangion, and N. Cressie (2022). Modeling nonstationary and asymmetric multivariate spatial covariances via deformations. *Statistica Sinica* 32(4), 2071–2093.
- Wadsworth, J. L. and J. A. Tawn (2014). Efficient inference for spatial extreme value processes associated to log-Gaussian random functions. *Biometrika* 101(1), 1–15.
- Wang, Y., M. Khodadadzadeh, and R. Zurita-Milla (2023). Spatial+: A new cross-validation method to evaluate geospatial machine learning models. *International Journal of Applied Earth Observation and Geoinformation* 121, 103364.
- Youngman, B. D. (2020). Flexible models for nonstationary dependence: Methodology and examples. *arXiv preprint arXiv:2001.06642*.
- Zammit-Mangion, A., T. L. J. Ng, Q. Vu, and M. Filippone (2022). Deep compositional spatial models. *Journal of the American Statistical Association* 117(540), 1787–1808.

Supplementary Material

This Supplementary Material contains further results pertaining to the simulation study (in particular estimated warpings for cases where the true warping is generated from Architectures 1, 2, and 4), as well as further results pertaining to the real data application (in particular, goodness-of-fit diagnostics confirming accuracy of the marginal tail model).

S7 Supplementary results for the simulation study

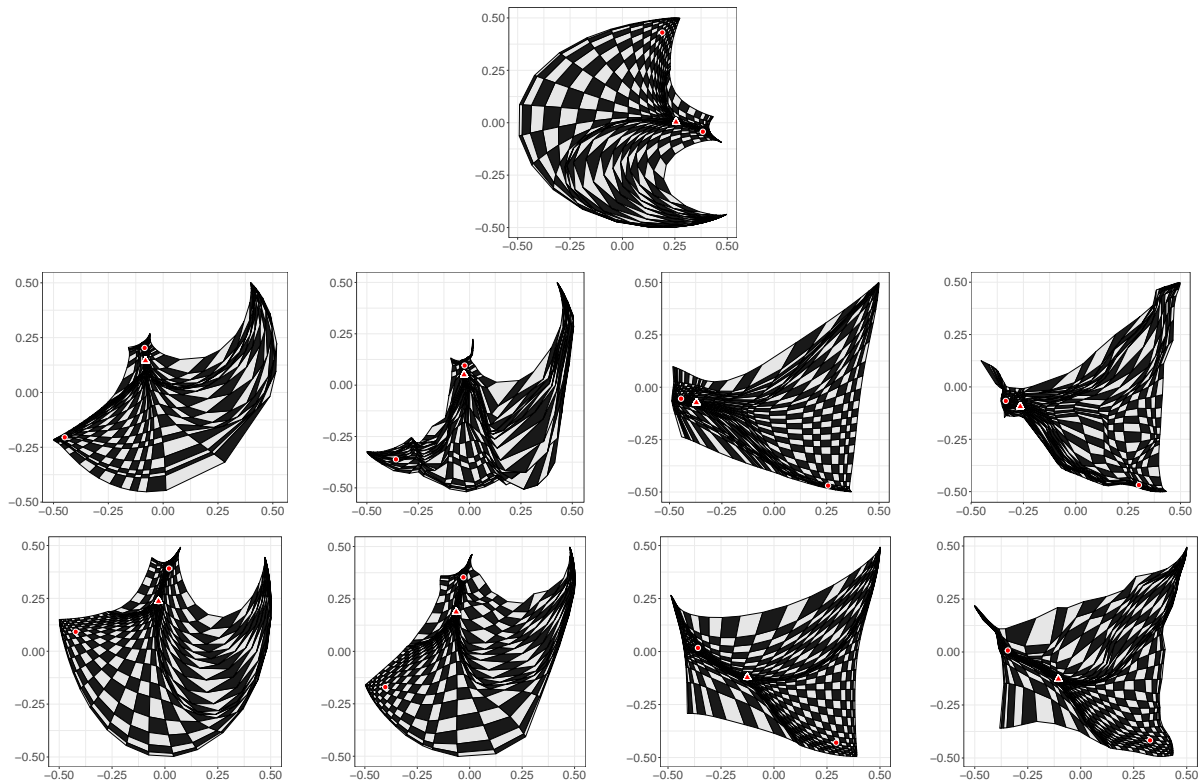


Figure S1: Top row: true warped domain \mathcal{W} generated using Architecture 1. Median and bottom rows: estimated warped space $\hat{\mathcal{W}}$ using nonstationary models 1–4 (column 1–4) with WLS and GSM inference methods, respectively. The data are generated with the risk functional $r_{\max}(\cdot)$, and three reference points are labeled in red.

Table S1: Test censored log-likelihoods (larger is preferred) evaluated for all fitted models, using both the gradient score matching (GSM) and weighted least squares (WLS) inference methods, and with three different risk functionals. The best models are highlighted in bold for each risk functional and each inference method, and the oracle model based on Architecture 1 is labeled with an asterisk.

Architecture	Inference method	Risk functional		
		$r_{\text{site}}(\cdot)$	$r_{\text{max}}(\cdot)$	$r_{\text{sum}}(\cdot)$
Stationary	WLS	-53326	-16726	17564
Nonstationary 1*		-50904	-14830	20936
Nonstationary 2		-51945	-15165	20944
Nonstationary 3		-51709	-16018	20252
Nonstationary 4		-50761	-15544	19048
Stationary	GSM	-53450	-16370	18269
Nonstationary 1*		-48205	-14179	22831
Nonstationary 2		-48258	-14222	22600
Nonstationary 3		-49048	-14589	22135
Nonstationary 4		-48882	-14480	22161

Table S2: Estimates of the extremal dependence parameters, $\hat{\psi} = (\hat{\varphi}, \hat{\kappa})$, for data generated with Architecture 1, using both the gradient score matching (GSM) and weighted least squares (WLS) inference methods, and three different risk functionals. The true values of the extremal dependence parameters are $\varphi_0 = 0.2$ and $\kappa_0 = 1$. Standard deviations obtained using a nonparametric bootstrap are reported in brackets as subscripts of the corresponding parameter estimate.

Architecture	Inference method	Risk functional		
		$r_{\text{site}}(\cdot)$	$r_{\text{max}}(\cdot)$	$r_{\text{sum}}(\cdot)$
Stationary	WLS	0.292 _(0.039) , 0.910 _(0.080)	0.518 _(0.169) , 0.995 _(0.145)	0.564 _(0.280) , 1.002 _(0.099)
Nonstationary 1		0.192 _(0.035) , 1.114 _(0.113)	0.225 _(0.082) , 0.886 _(0.143)	0.264 _(0.138) , 0.911 _(0.125)
Nonstationary 2		0.177 _(0.036) , 1.112 _(0.137)	0.245 _(0.075) , 0.902 _(0.129)	0.256 _(0.142) , 0.881 _(0.102)
Nonstationary 3		0.207 _(0.025) , 0.891 _(0.086)	0.350 _(0.087) , 0.970 _(0.149)	0.387 _(0.142) , 0.960 _(0.121)
Nonstationary 4		0.172 _(0.027) , 0.783 _(0.091)	0.305 _(0.077) , 0.909 _(0.139)	0.361 _(0.139) , 0.899 _(0.122)
Stationary	GSM	0.208 _(0.003) , 1.065 _(0.006)	0.209 _(0.003) , 1.067 _(0.006)	0.208 _(0.004) , 1.067 _(0.006)
Nonstationary 1		0.194 _(0.033) , 1.008 _(0.176)	0.195 _(0.030) , 1.016 _(0.158)	0.198 _(0.022) , 1.026 _(0.124)
Nonstationary 2		0.197 _(0.020) , 0.976 _(0.114)	0.193 _(0.017) , 1.017 _(0.098)	0.198 _(0.014) , 1.027 _(0.083)
Nonstationary 3		0.211 _(0.005) , 1.092 _(0.024)	0.212 _(0.003) , 1.107 _(0.021)	0.214 _(0.006) , 1.115 _(0.023)
Nonstationary 4		0.210 _(0.011) , 1.078 _(0.036)	0.200 _(0.007) , 1.075 _(0.032)	0.206 _(0.009) , 1.090 _(0.032)

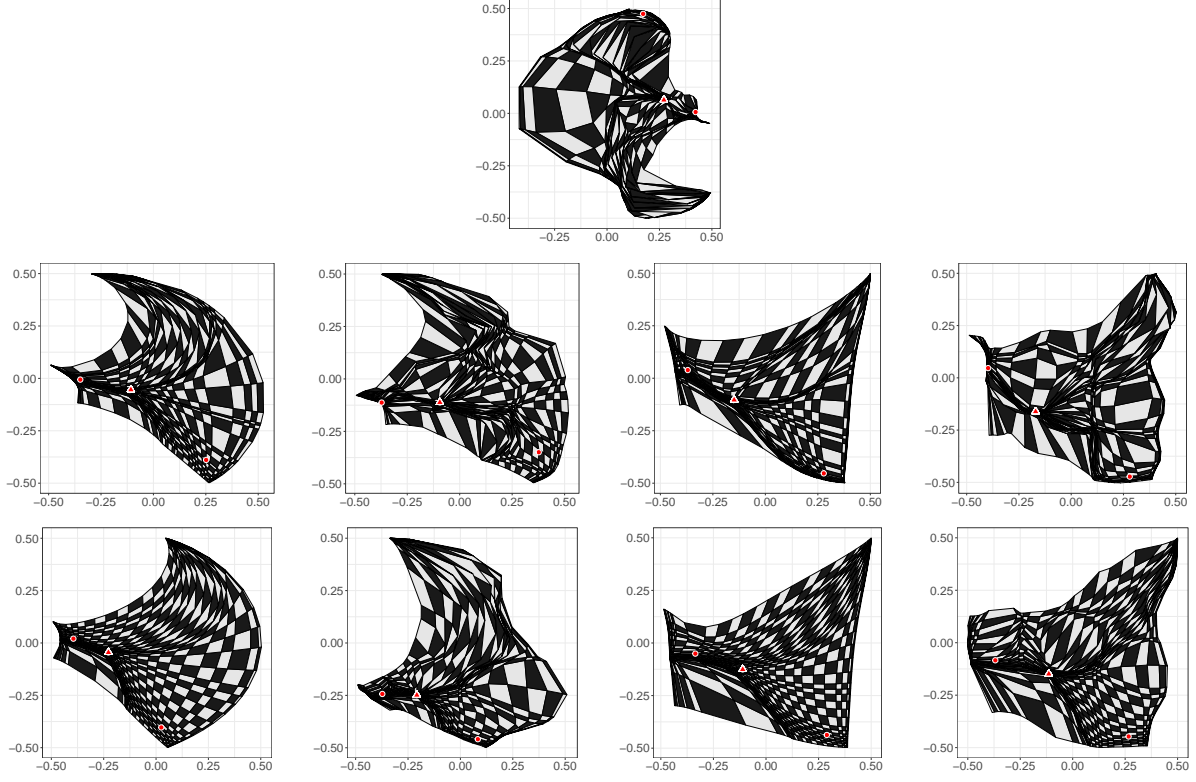


Figure S2: Top row: true warped domain \mathcal{W} generated using Architecture 2. Median and bottom rows: estimated warped space $\hat{\mathcal{W}}$ using nonstationary models 1–4 (column 1–4) with WLS and GSM inference methods, respectively. The data are generated with the risk functional $r_{\max}(\cdot)$, and three reference points are labeled in red.

Table S3: Test censored log-likelihoods (larger is preferred) evaluated for all fitted models, using both the gradient score matching (GSM) and weighted least squares (WLS) inference methods, and with three different risk functionals. The best models are highlighted in bold for each risk functional and each inference method, and the oracle model based on Architecture 2 is labeled with an asterisk.

Architecture	Inference method	Risk functional		
		$r_{\text{site}}(\cdot)$	$r_{\text{max}}(\cdot)$	$r_{\text{sum}}(\cdot)$
Stationary	WLS	−61754	−15506	24613
Nonstationary 1		−60598	−13895	28159
Nonstationary 2*		− 60162	− 13149	27396
Nonstationary 3		−64228	−13969	27887
Nonstationary 4		−71455	−13412	28873
Stationary	GSM	−59619	−15373	24283
Nonstationary 1		−55474	−13455	28320
Nonstationary 2*		−55363	− 13160	27624
Nonstationary 3		−56064	−13751	27750
Nonstationary 4		− 55141	−13358	28430

Table S4: Estimates of the extremal dependence parameters, $\hat{\psi} = (\hat{\varphi}, \hat{\kappa})$, for data generated with Architecture 2, using both the gradient score matching (GSM) and weighted least squares (WLS) inference methods, and three different risk functionals. The true values of the extremal dependence parameters are $\varphi_0 = 0.2$ and $\kappa_0 = 1$. Standard deviations obtained using a nonparametric bootstrap are reported in brackets as subscripts of the corresponding parameter estimate.

Architecture	Inference method	Risk functional		
		$r_{\text{site}}(\cdot)$	$r_{\text{max}}(\cdot)$	$r_{\text{sum}}(\cdot)$
Stationary	WLS	0.459 _(0.123) , 1.076 _(0.081)	0.322 _(0.064) , 1.126 _(0.087)	0.341 _(0.111) , 0.930 _(0.091)
Nonstationary 1		0.273 _(0.037) , 1.223 _(0.121)	0.198 _(0.030) , 1.151 _(0.114)	0.169 _(0.037) , 0.861 _(0.096)
Nonstationary 2		0.227 _(0.043) , 1.113 _(0.108)	0.200 _(0.032) , 1.076 _(0.105)	0.146 _(0.035) , 0.729 _(0.079)
Nonstationary 3		0.339 _(0.056) , 1.136 _(0.124)	0.234 _(0.042) , 1.122 _(0.126)	0.222 _(0.054) , 0.889 _(0.125)
Nonstationary 4		0.310 _(0.055) , 1.076 _(0.137)	0.206 _(0.042) , 1.014 _(0.114)	0.180 _(0.051) , 0.761 _(0.114)
Stationary	GSM	0.203 _(0.003) , 1.055 _(0.007)	0.201 _(0.002) , 1.050 _(0.005)	0.203 _(0.003) , 1.053 _(0.006)
Nonstationary 1		0.161 _(0.003) , 1.064 _(0.027)	0.166 _(0.009) , 1.080 _(0.084)	0.160 _(0.007) , 1.032 _(0.046)
Nonstationary 2		0.166 _(0.007) , 1.008 _(0.085)	0.162 _(0.018) , 0.983 _(0.128)	0.162 _(0.019) , 0.958 _(0.105)
Nonstationary 3		0.192 _(0.003) , 1.135 _(0.021)	0.193 _(0.009) , 1.114 _(0.134)	0.193 _(0.005) , 1.113 _(0.042)
Nonstationary 4		0.185 _(0.009) , 1.101 _(0.083)	0.188 _(0.014) , 1.107 _(0.135)	0.177 _(0.016) , 0.977 _(0.104)

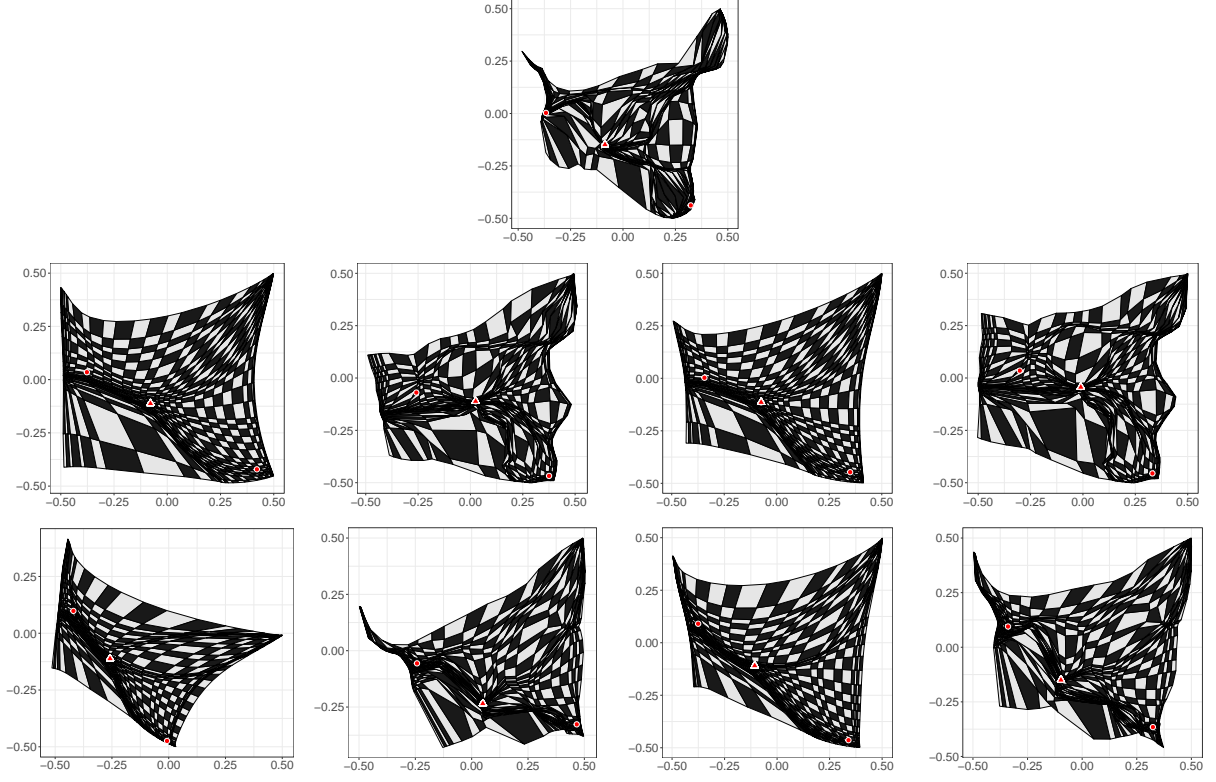


Figure S3: Top row: true warped domain \mathcal{W} generated using Architecture 4. Median and bottom rows: estimated warped space $\hat{\mathcal{W}}$ using nonstationary models 1–4 (column 1–4) with WLS and GSM inference methods, respectively. The data are generated with the risk functional $r_{\max}(\cdot)$, and three reference points are labeled in red.

Table S5: Test censored log-likelihoods (larger is preferred) evaluated for all fitted models, using both the gradient score matching (GSM) and weighted least squares (WLS) inference methods, and with three different risk functionals. The best models are highlighted in bold for each risk functional and each inference method, and the oracle model based on Architecture 4 is labeled with an asterisk.

Architecture	Inference method	Risk functional		
		$r_{\text{site}}(\cdot)$	$r_{\text{max}}(\cdot)$	$r_{\text{sum}}(\cdot)$
Stationary	WLS	-48545	-17247	14410
Nonstationary 1		-47919	-16227	16895
Nonstationary 2		-49704	-16086	17166
Nonstationary 3		-47666	-16050	16883
Nonstationary 4*		-46529	-16045	15549
Stationary	GSM	-46824	-16955	14716
Nonstationary 1		-44312	-15321	17661
Nonstationary 2		-42891	-15205	18258
Nonstationary 3		-44260	-15349	17697
Nonstationary 4*		-43179	-15226	18645

Table S6: Estimates of the extremal dependence parameters, $\hat{\psi} = (\hat{\varphi}, \hat{\kappa})$, for data generated with Architecture 4, using both the gradient score matching (GSM) and weighted least squares (WLS) inference methods, and three different risk functionals. The true values of the extremal dependence parameters are $\varphi_0 = 0.2$ and $\kappa_0 = 1$. Standard deviations obtained using a nonparametric bootstrap are reported in brackets as subscripts of the corresponding parameter estimate.

Architecture	Inference method	Risk functional		
		$r_{\text{site}}(\cdot)$	$r_{\text{max}}(\cdot)$	$r_{\text{sum}}(\cdot)$
Stationary	WLS	0.286 _(0.028) , 1.273 _(0.109)	0.314 _(0.048) , 1.145 _(0.068)	0.255 _(0.034) , 1.203 _(0.065)
Nonstationary 1		0.220 _(0.037) , 1.236 _(0.137)	0.213 _(0.034) , 1.129 _(0.099)	0.200 _(0.024) , 1.210 _(0.085)
Nonstationary 2		0.221 _(0.043) , 1.183 _(0.167)	0.228 _(0.040) , 1.131 _(0.119)	0.188 _(0.026) , 1.168 _(0.088)
Nonstationary 3		0.234 _(0.034) , 1.232 _(0.128)	0.262 _(0.032) , 1.137 _(0.098)	0.198 _(0.020) , 1.258 _(0.086)
Nonstationary 4		0.224 _(0.038) , 1.199 _(0.151)	0.247 _(0.035) , 1.158 _(0.117)	0.192 _(0.023) , 1.205 _(0.092)
Stationary	GSM	0.200 _(0.002) , 1.046 _(0.004)	0.199 _(0.002) , 1.043 _(0.003)	0.199 _(0.002) , 1.045 _(0.004)
Nonstationary 1		0.190 _(0.004) , 1.074 _(0.025)	0.189 _(0.003) , 1.076 _(0.015)	0.190 _(0.003) , 1.083 _(0.018)
Nonstationary 2		0.185 _(0.007) , 1.032 _(0.061)	0.182 _(0.015) , 1.029 _(0.135)	0.185 _(0.013) , 1.023 _(0.113)
Nonstationary 3		0.200 _(0.004) , 1.055 _(0.019)	0.195 _(0.003) , 1.041 _(0.013)	0.201 _(0.003) , 1.069 _(0.009)
Nonstationary 4		0.188 _(0.005) , 1.020 _(0.040)	0.192 _(0.006) , 1.036 _(0.050)	0.189 _(0.005) , 1.018 _(0.040)

S8 Supplementary results for the data application

S8.1 Modeling of margins

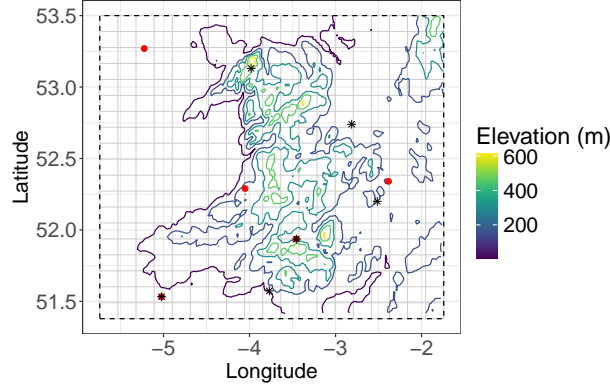


Figure S4: Geographical map of the study domain, with the position of five sites that violate the null hypothesis (labeled in red), namely that the data at these sites do not follow a GPD. We also display six representative sites (labeled as black stars; two of them correspond to the sites that violate the null hypothesis), which we use for goodness-of-fit checks.

For the marginal distributions, we assume that high quantile exceedances at each site are distributed as a generalized Pareto distribution (GPD) with scale and shape parameters (see Section 5.1 in the main article for details). To validate marginal fits, we compare the empirical tail distribution from the data and the fitted GPD model using quantile-quantile (Q-Q) plots (displayed on the Uniform(0, 1) scale) and Kolmogorov–Smirnov (K–S) distances. After fitting the marginal GPD to threshold exceedances, we obtain estimates $\hat{\tau}(\mathbf{s}_i)$ and $\hat{\xi}(\mathbf{s}_i)$ for all $i = 1, \dots, D$. Let $\hat{G}(\cdot) \equiv G(\cdot; \hat{\tau}(\mathbf{s}_i), \hat{\xi}(\mathbf{s}_i))$ be the estimated tail distribution at site \mathbf{s}_i , with $G(\cdot)$ as in (11) of the main article. If the marginal tail model is correctly-specified, $U_i = \hat{G}\{Y(\mathbf{s}_i) - u(\mathbf{s}_i)\}$ (with $u(\mathbf{s}_i)$ the selected marginal threshold) is approximately Uniform(0, 1) distributed, at each site. Thus, using Q-Q plots and K–S distances, we can check if $U_i \sim \text{Uniform}(0, 1)$.

Out of 12600 sites, only 5 reject the null hypothesis based on the K–S test. Q-Q plots for six representative sites (see Figure S4), which include two sites for which the null hypothesis is rejected, are shown in Figure S5. The Q-Q plots generally demonstrate good marginal

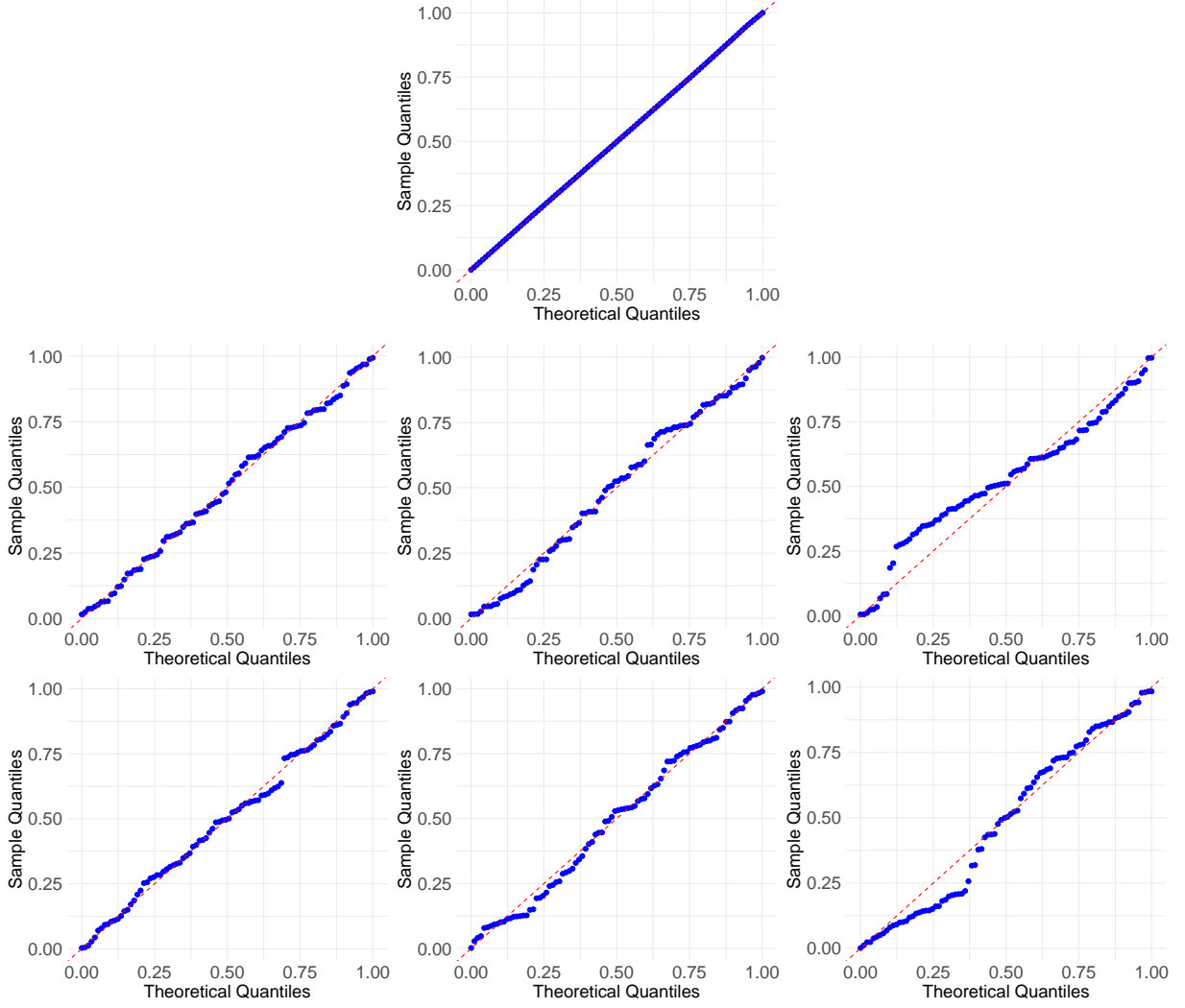


Figure S5: The quantile-quantile (Q-Q) plot of the marginal excesses for the total domain (top), and at six representative sites (labeled as black stars in Figure S4), where observations over four of them (the first and the second panels in the second and third rows) do not reject the null hypothesis that the data sampled there follow a GPD, and observations over the other two (the third panel in the second and third rows) which do reject the null hypothesis.

fits for the data at sites that do not reject the null hypothesis, i.e., the data sampled there follow a GPD, while some lack of fit is observed at sites that do reject the null hypothesis. Nevertheless, the fits appear to be quite satisfactory, even at these worst sites. We further display a Q-Q plot based on all the data from all sites pooled together. The results show that the marginal fit is very good overall.